Fakultät für Mathematik, Informatik,
Naturwissenschaften

Bachelor Thesis

Search for dark matter in proton-proton collision events with a muon and missing transverse energy in the CMS detector with $\sqrt{s} = 13$TeV

Pablo Martínez Agulló[1]

supervised by
Prof. Thomas Hebbeker

September 14, 2016

[1]University of Valencia

Abstract

In this thesis the search of dark matter is described by analyzing the transverse mass spectrum of proton-proton collisions events with one muon and missing transverse energy in the final state. Dark matter produced in the annihilation of two quarks is investigated. For this, three simplified models based on a mediator particle are used: axial vector, scalar and pseudoscalar. It is assumed that dark matter particles are weakly interacting massive particles. The search of this kind of matter is one of the main purposes of Large Hadron Collider. In this thesis we are using the data collected by the Compact Muon Solenoid during the Run II in 2015 with a center of mass energy of 13 TeV and integrated luminosity of 2.3 fb^{-1}.

As no significant deviation from the Standard Model predictions is seen, exclusion limits at 95% CL for the model parameters can be set. The sensitivity of this study is presented in terms of excluded mediator and dark matter masses for the models.

Contents

1 Introduction

Since the very first moment of our history, the humankind has pursued the knowledge of the nature. In fact the word physics comes from the Greek "φύσις" which means "nature". Firstly, the ancient Indian philosophers such as Kanada and Dignāga (6^{th} century BCE) and then the Greeks Democritus and Leucippus (5^{th} century BCE), developed the atomism, which comes from ἄτομον meaning "uncuttable" or "indivisible" [1] [2]. Since then, the search for the minute fragments that comprise the matter and its interactions has lead us to the standard model (SM) of particle physics.

The SM of particle physics is a theory of the structure of matter describing the properties of all known elementary particles and the forces between them. Studied experimentally for five decades, its predictions have been verified with very high precision. Despite the great success of the SM, beyond the SM (BSM) physics addresses a variety of open issues. To name a few examples: the relationship of the electroweak and gravitational energy scales must be understood and incorporated in the theory, an underlying concept is needed to explain the origin of the observation of only three fermion families, the neutrino oscillations and the matter antimatter asymmetry are not explained in the SM, astrophysical observations indicate the presence of Dark Matter (DM) not described in the standard model. The last one is the main subject of this thesis.

Currently the DM is among the most important open problems in modern physics, especially in particle physics, as witnessed by the enormous theoretical and experimental effort that is being put towards its identification. Despite observational evidence such as the galaxy rotation curves or the gravitational lensing, it has not yet been detected and its structure and physical behavior at the subatomic level are still unknown. To achieve an answer, the Large Hadron Collider (LHC) is expected to provide insights of paramount importance into possible extensions of the SM of particle physics.

In this work, events with a muon and missing transverse energy (E_T^{miss}) are examined using the Compact Muon Solenoid (CMS) detector. The muon and E_T^{miss} final state has a distinct event signature, constituted from only one identified particle. One or more particles in the event remain undetected but their incidence can be reconstructed from the total transverse momentum in the event. This is a promising search channel in terms of the discovery of new physics. The E_T^{miss} can originate from neutrinos, but also from new unknown particles such as DM particles. The clear signature of the channel does not require complicated selection criteria and it has a well understood SM background

Three different models for DM production, distinguished in structure and how the mediator couples to the particle, will be compared: axial vector (AV), scalar (S) and pseudoscalar (P) model. With a Monte Carlo (MC) generator, those three processes are simulated in the CMS system for a center of mass energy of 13 TeV and then compared to the data collected from CMS in 2015 and the background simulations to verify if they are compatible.

The thesis is structured in five main sections and the appendix. In the following the theoretical aspects are studied from the SM to the simplified models. In the third section the setup of the experiment is described in detail. The proton-proton collision data at $\sqrt{s}$= 13 TeV is interpreted in terms of DM in section 4. Finally, a summary of the results can be found on section 5.

2 Theoretical framework

2.1 Standard Model

The SM of particle physics is a theory concerning the electromagnetic, weak, and strong nuclear interactions, also classifying all known subatomic particles. It was developed throughout the latter half of the 20^{th} century as a collaborative effort of scientists around the world. The formulation was finalized in the 1970s upon experimental confirmation of the existence of quarks. Since then, discoveries of the top quark (1995 at Fermilab), the tau neutrino (first detected in 2000 at Fermilab [3]) and, more recently, the Higgs boson (first detected in 2012 at CERN), have given further credence to the standard model.

In the SM there are two different types of particles: fermions and bosons. While the former have a half-integer spin, the latter are characterized by integer spins. The fermions are divided into leptons and quarks. The fermions are divided in three generations or families, one for each column in Fig. 1. Each fermion has an antiparticle (except neutrinos, which could their own antiparticle). Bosons are the mediators of the four fundamental interactions described by SM; the electromagnetic force is transmitted via photons, the weak force is mediated by W^+, W^- and Z^0 bosons between particles of different flavors[2] and the eight gluons mediate the strong interactions between color[3] charged particles. The Higgs boson is different from the ones mentioned before since it does not transmit a fundamental force and is the responsible for rest mass.

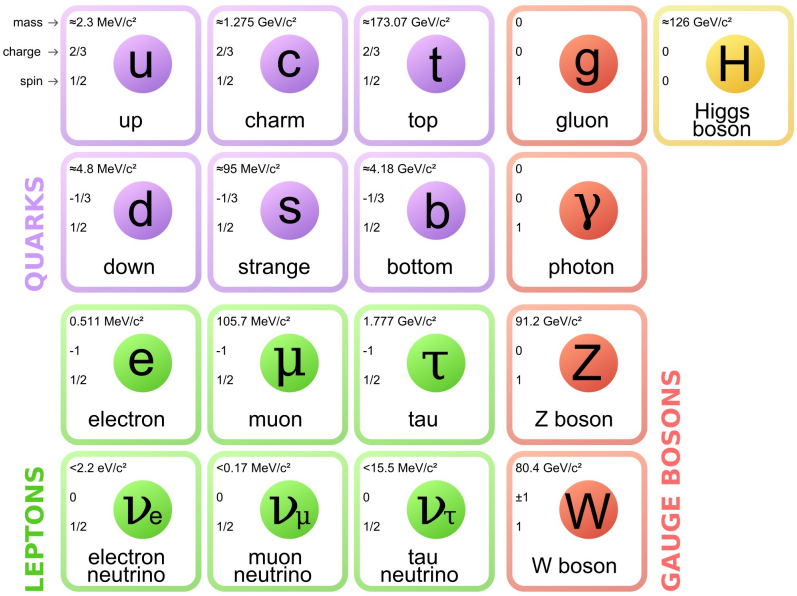

Figure 1: Standard model of particle physics [4].

[2]There are six different quark flavours (u,d,c,s,t and b) and six lepton flavours (e,μ,τ,ν_e,ν_μ and ν_τ).
[3]Color is the strong interaction analog to charge in the electromagnetic force.

2.2 Dark Matter

Nowadays, dark matter (DM) composes 26.8% of the mass-energy of the universe. The rest corresponds to the ordinary matter, 4.9%, and dark energy, 68%. This implies that DM is 84.5% of the total mass of the universeAstrophysical observational evidence of its existence combined with the fact that it has not yet been found, makes the DM one of the most interesting fields in particle physics. The most widely accepted hypothesis on the composition for DM proposes that it is composed of weakly interacting massive particles (WIMPs) that interact only through gravity and the weak force.

2.2.1 Observational evidences

The most important evidences of the existence of DM are due to astrophysical observations and cosmology models such as the Λ-CDM model. Here are shown the most relevant ones.

Galaxy rotation curves

The first one who postulated the presence of far more mass than anyone had previously predicted was J.H. Oort in 1932. He calculated the velocity of the stars moving near the galactic plane and realized that they were moving quickly enough to escape the gravitational pull of the luminous mass of the galaxy. However, he assumed that either his velocity measurements were wrong or that the expected mass that he had measured was obscured by the dust leading to an underestimation of the visible mass. [5]

The next year the Swiss astronomer F. Zwicky studied the Coma cluster, which is about 99 Mpc from Earth, and used the virial theorem to calculate the mass of the cluster, finding that it was $M_{Cluster} \approx 4.5 \times 10^{13} M_{\odot}$. Since he observed approximately 1000 galaxies in the cluster, he calculated that the average mass of each galaxy should be $M_{Galaxy} \approx 4.5 \times 10^{10} M_{\odot}$, which was somewhat unexpected in view of the fact that the luminosity of an average nebula is nearly $8.5 \times 10^{7} L_{\odot}$ and he had approximately $5 \times 10^{9} L_{\odot}$. With this he inferred the existence of unseen or "non-luminous" matter that he named *dark matter*, which was the vast majority of the mass of the cluster, about 4000 more mass [6] [7]. The gravitational value of the mass that he obtained was at least 400 times greater than expected from their luminosity.

Four decades after Zwicky's measurements, the American astronomer Vera Rubin studied the rotation curves –Fig. 2 Left– of sixty isolated galaxies and she found an extreme deviation from the predictions due to Newtonian gravity and the visible mass. Her measurements showed that the rotational velocity remained constant with increasing galaxy radius; therefore the mass inside this radius should increase. Since the luminous mass is in the center of the galaxy, the missing mass must be non-luminous and not concentrated near the center [8]. This was the strongest indication up to that time for the existence of DM.

Gravitational lensing

By the same time that Rubin made her research, another piece of evidence to prove the existence of DM was discovered; the gravitational lensing. As a result of Einstein's Theory of Relativity, which postulates that the universe is a flexible fabric of space time that can be bent by objects with mass affecting the motion of the bodies around them, the path of light is affected when encountering massive objects and this produce that the DM behaves like an optical lens. An example for the gravitational lensing due to DM –Fig. 2 Right– is the cluster Abell 370 [9].

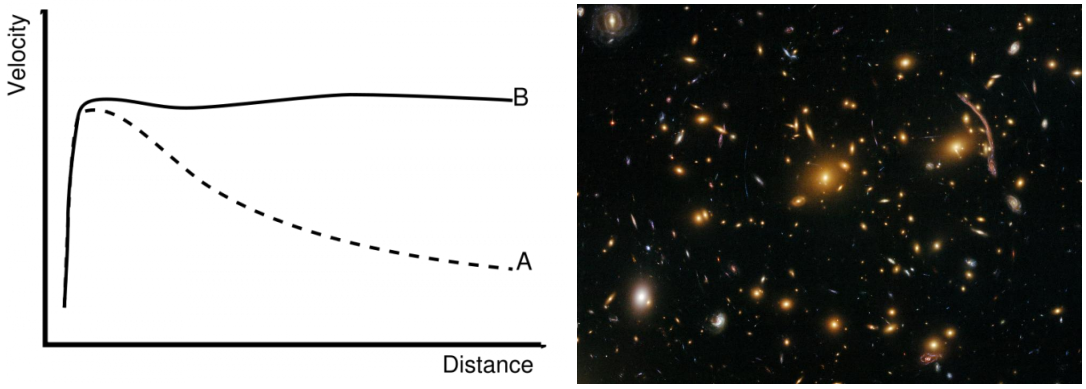

Figure 2: Left: Rotation curve of a typical spiral galaxy, showing the speed in the galactic plane as a function of the distance from the galactic nucleus. (A) The dashed line corresponds to keplerian predictions. (B) The continuous line is the observed. The discrepancy between both curves can be accounted for by adding a dark matter halo to the galaxy [10]. Right: Gravitational Lensing in Galaxy Cluster Abell 370. Credit: NASA, ESA, the Hubble SM4 ERO Team, and ST-ECF.

Cosmic Microwave Background

The cosmological evidence is due to anisotropies in the Cosmic Microwave Background (CMB). The CMB –Fig. 3– was discovered by Penzias and Wilson in 1964 as and excess background temperature of about 2.73 K. The satellite named Cosmic Background Explorer (COBE), also referred as Explorer 66, found that CMB is remarkably uniform but it has some fundamental anisotropies. The fluctuations in the CMB temperature are dependent of the amount of baryons in the universe at the time of recombination, when the neutral atoms were formed and the universe became transparent to the electromagnetic radiation leading to the CMB. This is known as photon decoupling. The COBE results showed a need for an electrically neutral form of matter that could been properly structured before the time recombination [11].

The density parameter, $\Omega = \frac{\rho}{\rho_C}$ where ρ_C is the density that would cause the universe to expand forever, is composed by the sum of the mass density, the effective mass density of relativistic particles (light and neutrinos) and the effective mass density of the dark energy: $\Omega = \Omega_m + \Omega_{rel} + \Omega_\Lambda$. The mass density parameter includes ordinary (baryonic) matter and the DM. The most recent results of Ω_m correspond to the measurements of CMB done by the Planck space observatory from ESA, which substantially improved the observations of the Wilkinson Microwave Anisotropy Probe (WMAP). The measured total and baryonic mass densities are $\Omega_m = 0.313 \pm 0.013 \rightarrow \Omega_m h^2 = 0.1426 \pm 0.0020$ and $\Omega_b h^2 = 0.02222 \pm 0.00023$. Therefore, the baryonic matter is not the only form of matter in the universe; the DM density, $\Omega_{DM} h^2 = \Omega_m h^2 - \Omega_b h^2$, is around the 85% of the total density mass. [12]

In conclusion, more than 80 years since the Zwicky's calculations have passed and an abundance of observations have confirmed the existence of dark matter on a wide range of scales. More recent evidences come from the Bullet cluster and MACS J0025.4-1222 galaxy cluster. [13] [14]

2.2.2 Dark Matter candidate

Today there is broad consensus that DM is made by new particles. However, DM remains one of the outstanding mysteries in modern particle physics, astrophysics, and cosmology.

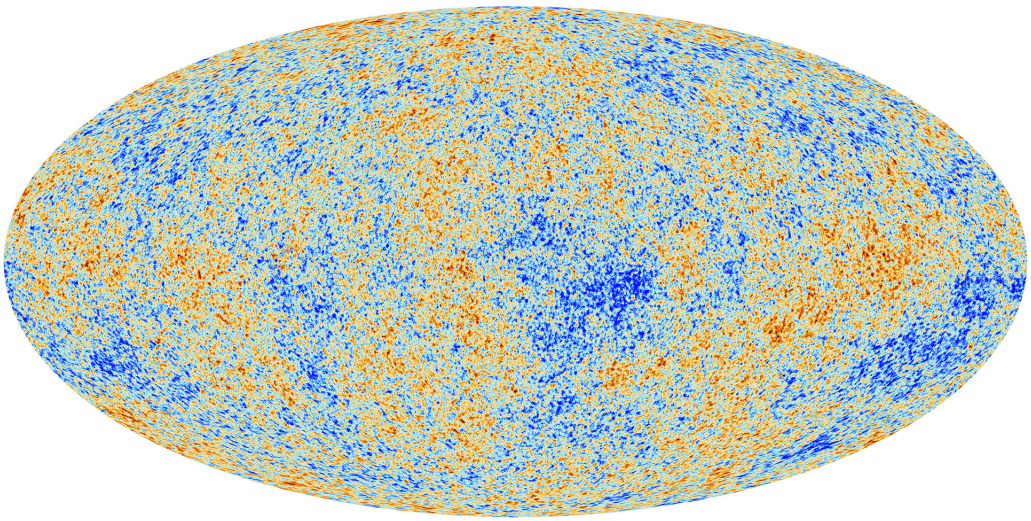

Figure 3: The anisotropies of the Cosmic microwave background (CMB) as observed by Planck. The CMB is a snapshot of the oldest light in Universe and it shows tiny temperature fluctuations that correspond to regions of slightly different densities, representing the seeds of all future structure: the stars and galaxies of today. Copyright: ESA and the Planck Collaboration.

The most accepted hypothesis states that the DM is made of WIMPs such as neutralino, GeV neutrino, technicolor particle, extra Higgs, etc [15]. There other candidates like axioms or light neutrinos but these are not discussed in this work. WIMPs are a broad category of DM candidates with a particular set of properties: they couple to the SM via weak interactions and are thermally produced in the early universe with their relic density set by their abundance when they freeze out. W Imp's name comes from the fact that obtaining the correct abundance of dark matter today via thermal production requires a self-annihilation cross section of $< \sigma v > \approx 3 \times 10^{-26}$ cm^{3}s^{-1}, which is roughly what is expected for a new particle in the 100 GeV mass range that interacts via the weak force [11]. Because supersymmetric extensions of the SM of particle physics readily predict a new particle with these properties, this apparent coincidence is known as the "WIMP miracle", and a stable supersymmetric partner has long been a prime WIMP candidate. [16]

The DM candidate searched for in this thesis is a WIMP. From an experimental point of view, what is most important is that WIMPs only interact weakly and gravitationally so they leave the detector without being detected. Thus any search for DM has to be produced along other particles which are detectable, named tagging particles. The search signature of this analysis is the mono-μ channel, which is subsequently discussed.

It could be possible that the DM is not a fundamental particle but a structure. In this case, the simplification of assuming it like a particle is reasonable because one mediator or decay channel could play a dominant role [17].

2.2.3 Alternative theories

The existence of DM has not been proved and, despite all the evidences we have, there are several scientists that do not rely in it. There are two reasons for thinking abut other theories. Firstly, if our understanding of gravity on the astronomical scales is incorrect or flawed, the demands of the existence of DM by astronomical observations is in risk. Secondly, DM has not been directly identified yet by means of a nongravitational experiment.

The alternative theories for explaining the previous observational evidences without leaning on the notion of DM call for a relativistic modified theory different from general relativity.

One of the most popular alternative theories for providing a DM free explanation for the galaxy rotation curve problem are the MOND (MOdifed Newtonian Dynamics) theories. They are based in an acceleration constant a_0 to modify Newton's second law, which would, at small accelerations, account for the radius independent nature of stellar motion. In the context of MOND, the force acting on an object of mass m and acceleration $a = |\overrightarrow{a}|$ is $\overrightarrow{F} = m\mu\left(\frac{a}{a_0}\right)\overrightarrow{a}$, where $\mu(a/a_0)$ is a still unspecified function that behaves like $\mu(a/a_0 >> 1) \approx 1$ and $\mu(a/a_0 << 1) \approx a/a_0$ with $a_0 \approx 2 \times 10^{-8}$ cm s^{-2}. The gravitational force is, therefore $\overrightarrow{F} = \frac{GMm}{r^2} = m\mu\left(\frac{a}{a_0}\right)\overrightarrow{a}$. For large r we can assume that $\mu(a/a_0) = a/a_0$. So, $\frac{GM}{r^2} = \frac{a^2}{a_0} \rightarrow a = \frac{\sqrt{GMa_0}}{a_0} = \frac{v^2}{r}$, and therefore $v = \sqrt[4]{GMa_0}$. This last equation shows for the speed in the galactic plane is not the pendent on the distance from the galactic nucleus, explaining the galaxy rotation curve –Fig. 2.2.1 Left– flatness. Nevertheless, the MOND theories do not explain the gravitational lensing.

Another theories consider mass in extra dimensions instead of DM. Instead of using DM, other masses can be considered. In some multidimensional theories the gravitational force is the only one with effect across all dimensions. This explains the relative weakness of gravity compared to the other forces of nature that cannot cross into extra dimensions [18]. In that case, the mass that acts like DM could exist in a "Hidden Valley" in other dimensions that only interact with the matter in our dimensions through gravity.

2.3 Dark Matter production model

Our knowledge of DM and its physical properties is very small and some assumptions about DM particles have to be done. During this analysis the DM particle is considered to act like a fermion because if it acted like a boson it would have a smaller cross section and it would not be able to be detected at LHC at the moment; furthermore the astrophysical measurements favor this choice [12].

Regardless the dark sectors of the BSM physics can be complex, mediators are one possibility for explain its production; DM particles can interact with visible matter by the exchange of a mediator [19].

DM hadron collider productions mechanisms are discussed emphasizing the distinctive mono-μ channel. When we consider a process with hadron-hadron collision, protons in our case, in an accelerator the mediator (referred as "med") is initially produced and, afterwards, it decays into SM particles or into DM particles. In the latter channels we will have missing transverse energy (E_T^{miss}). Fig. 4 shows the final state that is analyzed.

2.3.1 Mono-μ channel

A pair of DM particles that are produced in a collider with a final state $\mu + E_T^{miss}$ are studied. This muon comes from a W boson that decays into a muon and a neutrino.

This kind of collision is called mono-μ channel and it present several advantages. First of all, the single lepton channels like the mono-μ have a very clear signature in the electromagnetic calorimeter or the muon chamber, and a possibly very large E_T. Secondly, the SM background is known and it mostly consists in W bosons decays. Other background processes to be considered are the $t\bar{t}$ and single t production, Drell-Yan and diboson processes. A more detailed study of the background is done on Section 4.3.

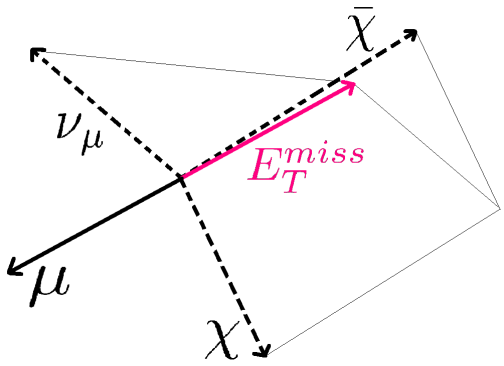

Figure 4: Representation of the final state. The dashed lines represent the p_T of the particles that are not detected and its sum is E_T^{miss}.

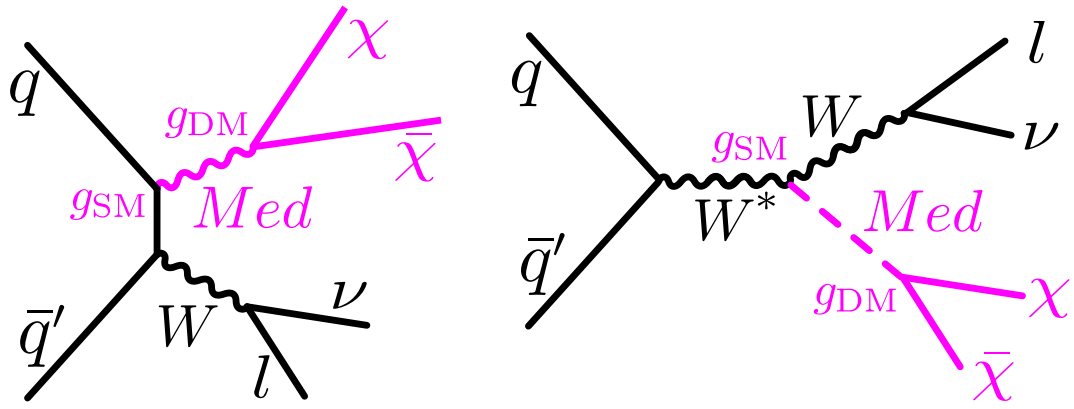

Figure 5: Feynman graph of DM production simplified models for the mono-μ channel. Left: Exchange of an axial-vector or vector coupling mediator particle. Right: Exchange of a scalar or pseudo-scalar coupling mediator particle. If wit is a $\bar{l} + \nu$ decay the SM boson is W^+ and if it is a $l + \bar{\nu}_l$ then it is a W^-.

There are others mono-X channels such as mono-W, mono-jet, mono-γ or mono-Z. All these channels provide different features, advantages and disadvantages. The mono-γ and mono-jet searches have a huge background in the detector compared to the mono W. These two channels have nevertheless high cross section, because of the large influence from strong interaction processes to the total cross sections in a collider at high energies.

2.3.2 Simplified models

The models that are used in this thesis for describing the DM production are known as simplified models and are characterized by the existence of a mediator field. This mediator can couple differently, like an axial vector (AV), vector (V), scalar (S) or pseudoscalar (P). In the Fig. 5 the difference between V or AV couplings and S or P couplings is shown. While the V and AV mediators are coupled to the quark, the S and P are coupled to the boson[4].

[4]The vector coupling is not discussed in the analysis because former analyses have shown that AV and V coupling processes does not differ significantly. [20]

The Vector and Axial Vector Models

In previous works, the two models that have been studied in more detail are the AV mediator and the V. The axial-vector coupling is spin dependent while the vector coupling is spin independent. This is important in light of direct detection. For the W channel it makes no difference since once W requires polarized quarks. Previous analysis have shown that the difference in cross section between the AV and V models is no significant [20]. Therefore, for minimizing the computation efforts just one of those two models –Fig. 5 Left– is being discussed, the AV. This choice is made because, in the generator search, we can set superior limits compared to direct detection experiments. For the vector only coupling mediator, where the direct detection is a real competition to this analysis, this is not the case.

The Lagrangians for the V and AV models are respectively:

$$\mathcal{L}_V = -g_q \sum_{q=u,d,s,c,b,t} Z'_\mu \bar{q}\gamma^\mu q - g_{DM} Z'_\mu \bar{\chi}\gamma^\mu \chi \tag{2.1}$$

$$\mathcal{L}_{AV} = -g_q \sum_{q=u,d,s,c,b,t} Z'_\mu \bar{q}\gamma^\mu\gamma^5 q - g_{DM} Z'_\mu \bar{\chi}\gamma^\mu\gamma^5 \chi \tag{2.2}$$

For discussing the impact of the mediator on the our AV and V simplified models we define the minimal widths as functions of the partial width of the mediator decay to DM and the mediator decay to the considered quarks:

$$\Gamma^{V,AV}_{med,min} = \Gamma^{V,AV}_{\chi\bar{\chi}} + \sum_{i=1}^{N_f} N_c \Gamma^{V,AV}_{q_i\bar{q}_i} + N_c \Gamma^{V,AV}_{t\bar{t}} \tag{2.3}$$

Where the fermionic partial decay width ($\Gamma_{f\bar{f}}$) depending on the coupling is given by:

$$\Gamma^{V}_{f\bar{f}} = \frac{g_f^2 (M^2_{med} + 2m_f^2)}{12\pi M_{med}} \sqrt{1 - \frac{4m_f^2}{M^2_{med}}} \tag{2.4}$$

$$\Gamma^{AV}_{f\bar{f}} = \frac{g_f^2 (M^2_{med} - 4m_f^2)}{12\pi M_{med}} \sqrt{1 - \frac{4m_f^2}{M^2_{med}}} \tag{2.5}$$

with f denoting either a SM quark or DM particle.

The Scalar and Pseudoscalar Models

In the scalar model, the mediator is assumed to act like a scalar particle and the Lagrangian is:

$$\mathcal{L}_S = a\phi\bar{\psi}\psi \tag{2.6}$$

The Higgs boson is the only known scalar elementary particle by now.

On the other side, in the pseudoscalar model, the mediator is assumed to act like a pseudoscalar particle. The Lagrangian is:

$$\mathcal{L}_{PS} = b\phi\bar{\psi}\gamma_5\psi \tag{2.7}$$

Which is quite similar to the scalar one but with the Dirac matrix γ_5. There are no elementary pseudoscalar particles discovered and they would be CP violating. The most known pseudoscalar particle is the neutral pion, π^0.

These channels ares shown in Fig. 5 (Right). The effective field operators are:

$$\text{Scalar coupling: } -\frac{1}{2}M_{med}^2 S^2 - g_{DM} S \bar{\chi}\chi \tag{2.8}$$

$$\text{Pseudocalar coupling: } -\frac{1}{2}M_{med}^2 P^2 - g_{DM} P \bar{\chi}\gamma^5\chi \tag{2.9}$$

The scalar mediator coupling width is:

$$\Gamma_{med}^S = \Gamma_{\chi\bar{\chi}}^S + \Gamma_{WW}^S \tag{2.10}$$

with partial decay widths $\Gamma_{\chi\bar{\chi}}^S$ and Γ_{WW}^S of the form:

$$\Gamma_{\chi\bar{\chi}}^S = \frac{g_{DM}^2 4M_\chi^2 M_{med}}{8\pi v^2}\left(1 - \frac{4M_\chi^2}{M_{med}^2}\right)^{\frac{3}{2}} \tag{2.11}$$

$$\Gamma_{WW}^S = \frac{m_w^4}{4\pi M_{med} v^2}\sqrt{1 - \frac{4M_{med}^2}{m_W^2}}\left(3 + \frac{M_{med}^4}{4m_W^4} - \frac{M_{med}^2}{m_W^2}\right) \tag{2.12}$$

And for the pseudoscalar mediator, an approximation of its decay width is determined from equation 2.12:

$$\Gamma_{med}^P \approx \Gamma_{\chi\bar{\chi}}^P + \Gamma_{WW}^S \tag{2.13}$$

$$\Gamma_{\chi\bar{\chi}}^P = \frac{g_{DM}^2 M_\chi^2 M_{med}}{8\pi v^2}\left(1 - \frac{4M_\chi^2}{M_{med}^2}\right)^{\frac{1}{2}} \tag{2.14}$$

There is no coupling of mediator to SM particle at tree level. Otherwise, the coupling structure would have to be CP-violating [21].

2.3.3 Simplified model parameters

In the simplified model the mediator is characterized by the production mechanism and by the model parameters. The parameter space is defined four parameters:

- M_{med} - mediator mass.
- M_χ - DM particle and antiparticle mass (also referred as m_{DM}).
- g_{SM} - coupling strength between the mediator and a quark or the W boson.
- g_{DM} - coupling strength between the mediator and the DM.

In our analysis the coupling strength to the mediator is the same for DM and the quark and W boson, $g_{DM} = g_{SM} = 1$.

Both Feynman diagrams of Figure 5 can be understood as an s-channel if only the DM part is considered. The cross section for an s-process is proportional to [22]:

$$\sigma_{pp\to\chi\bar{\chi}+X} \propto \frac{g_{SM}^2 \cdot g_{DM}^2 \cdot q^2}{(q^2 - M_{med}^2)^2 + q^2\Gamma_{med}^2} \tag{2.15}$$

where $\Gamma_{med}(M_{med}, M_\chi, g_{g/W}, g_{DM})$ is the mediator width and q is the momentum exchange in which the mediator is involved [23]. A larger emphasis is laid on smaller width since the LHC is more sensitive, because $\sigma \propto \Gamma^{-2}$.

The g_{SM} and g_{DM}, besides of modifying the $\sigma_{pp\to\chi\bar{\chi}+X}$, affect to the kinematics of the process. Perturbation theory requires that the mediator width has to be roughly smaller than a half of its mass: $\Gamma_{med} < \frac{M_{med}}{2}$ but typically is used a more conservative value of $\Gamma_{med} \lesssim \frac{M_{med}}{3}$. This is a guideline for an upper bound of the mediator width.

Mediator width

The total width is a sum over all possible partial widths decay of the mediator, $\Gamma = \sum_j \Gamma_j$. It can have a decay to quarks, $N_c \cdot \Gamma_{(med\to q_i q_i)}$, or to DM, $\Gamma_{(med\to\chi\bar{\chi})}$. N_c is the color factor of the quarks (there are 3 different possible color for them) and the i in q_i stand for the 6 different quark flavors. The case of the top quark should taken in special consideration for being the heavier, as equation 2.3 shows. If the mediator mass is lower than twice the fermionic mass we have a negative number as argument for the square root in the equations 2.4 and 2.5.

In the further analysis two situations regarding to the width are studied: narrow width, $\Gamma = \frac{M_{med}}{8\pi}$, and conservative width, $\Gamma = \frac{M_{med}}{3}$. The former one corresponds to the case in which the $q_i = u$ and the $N_c = 1$, and the latest represents $q_i = u, d, s, c, b, t$ and $N_c = 3$.

3 Experimental setup

There are three different approaches –Fig. 6– for the detection of DM particles; direct and indirect detection and production at colliders. Direct detection experiments search for the scattering of DM particles with SM model particles, while in indirect detection the products of the WIMP annihilation are seen.

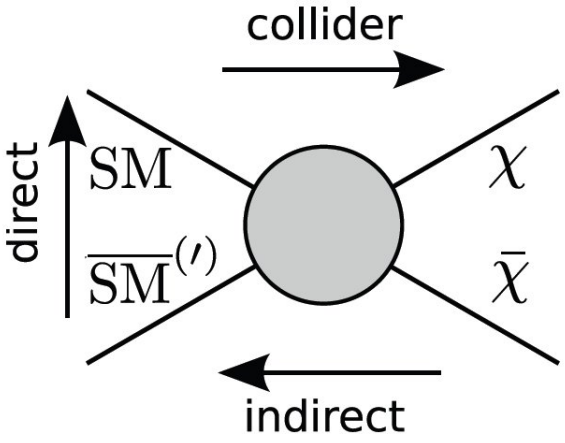

Figure 6: Feynman representation of the three detection schemes. The direction indicated above each name represents the time arrow for this approach. [21]

In this thesis we study the detection in colliders. The experiment consists in producing WIMPs in the laboratory with proton collisions and identify the DM particles by the measurement of the other particles produced at the same time. The detector used in for this analysis is the CMS, which is described in the next sections. As explained in 2.3, the particles that are hypothetically produced in our model are a μ, a ν_μ and a DM paticle-antiparticle pair (χ, $\bar{\chi}$), however from these four particles the only one that we can detect is the muon.

The experimental setup is located at the facilities of The European Organization for Nuclear Research, best know by CERN (this acronym comes from the provisional name that it had in 1965, *Conseil Européen pour la Recherche Nucléaire*. Located in Geneva, it is the largest particle physics research laboratory in the world.

3.1 Large Hadron Collider

This section is based on [24].

The Large Hadron Collider (LHC) is the largest and most energetic particle accelerator existing nowadays. It is a two-ring superconducting hadron accelerator and collider installed in the 26.7 km tunnel that was constructed between 1984 and 1989 for the CERN Large Electron-Positron (LEP) machine. It first started on September 2008 and remains the latest addition to CERN's accelerator complex, in Geneva.

The accelerator consists of two rings with oppositely oriented proton beams. Those beams are accelerated by different radiofrequency (RF) cavities, which requires that the injected protons already have a high velocity. An accelerator chain –Fig. 7– composed of the Linac 2, the Proton Synchrotron Booster (PSB), the Proton Synchrotron (PS) and finally the Super Proton Synchrotron (SPS) is used to achieve the necessary speed. Then the particles are injected in the LHC pipes, which consist in two ultrahigh vacuum tubes. The protons are kept in the pipes with dipoles and quadrupoles and are guided by a strong magnetic field maintained by superconducting electromagnets. These include 1232 dipole magnets 15

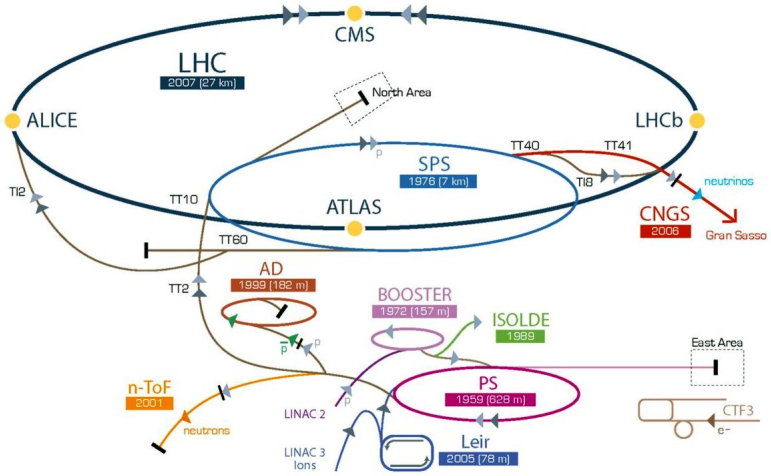

Figure 7: Scheme of LHC including the acceleration chain. [27]

meters in length which bend the beams, and 392 quadruple magnets, each 5–7 meters long, which focus the beams.

It was constructed for reaching a maximum center of mass energy ($\sqrt{s}$) of 14 TeV and a peak instantaneous luminosity of $\mathscr{L} = 10^{34}$ cm^{2}s^{-1}, in June 2016 peak luminosity exceeded this amount [25]. The proton beams are bunched with a bunch-to-bunch distance of 25 ns. This corresponds to a maximum bunch crossing frequency of 40 MHz.

The LHC is divided into eight sections (points), with a cavity each one, to potentially install new detectors and run experiments on them. There are two high luminosity general propose experiments, ATLAS and CMS , both aiming at a peak luminosity of $\mathscr{L} = 10^{34}$ cm^{2}s^{-1} for proton operation. There are also two low luminosity experiments: LHCb for b-physics, aiming at a peak luminosity of $\mathscr{L} = 10^{32}$ cm^{2}s^{-1} and ALICE $\mathscr{L} = 10^{30}$ cm^{2}s^{-1}. Other experiments are: TOTEM, LHCf and MoEDAL [26].

3.1.1 Run II

At the beginning of 2013 the LHC stopped in order to work on maintenance tasks and improvements that allow an increment of the beam energies, after three years operating and producing protons collisions at center of mass energies of 7 and 8 TeV. Last year it started to run again at an energy of 13 TeV, almost twice its previous energy. This is known as Run II.

Now there are less protons per bunch; $1.2 \cdot 10^{11}$ compared to the $1.7 \cdot 10^{11}$ in 2012. With this decrease, the computation systems can more easily distinguish which particle comes from every collision. This is allude to the pileup events, which are the different separate events that are produced by the same bunch crossing in high-luminosity colliders. The frequency of collisions has been improved to 25 ns from 50 ns.

3.2 Compact Muon Solenoid

Unless state otherwise, this section is based on [28].

The Compact Muon solenoid (CMS) –Fig. 8– is one of the two multipurpose detectors of the LHC. It is named *Compact* because despite having a smaller volume than ATLAS it has a larger mass, *Muon* because it is specially optimized for detecting muons and *Solenoid* because it has a high-field solenoid magnet. The detector is built around one collision point.

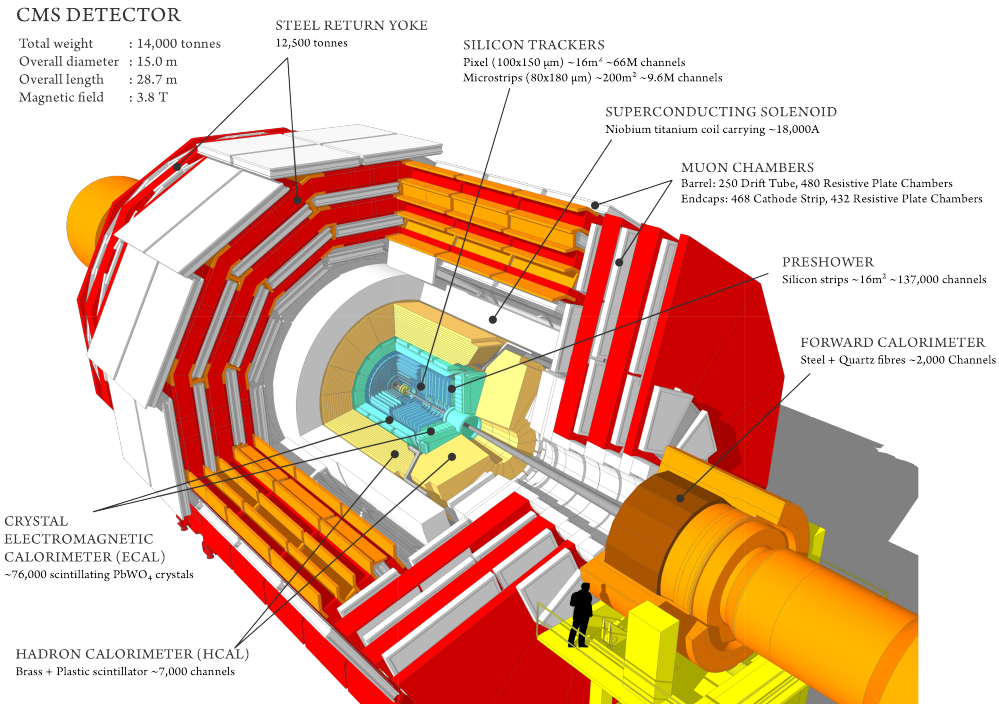

Figure 8: Sectional view of the CMS detector. The LHC beams travel in opposite directions along the central axis of the CMS cylinder colliding in the middle of the detector [29].

Particles transversing the CMS leave signals in the different layers. Allowing the particles to be identified.

A high magnetic field sits at the core of the CMS detector. A large bore superconducting solenoid is surround a silicon tracker, constructed from scintillating crystals, an electromagnetic calorimeter and a hadron calorimeter, build as sampling calorimeter. The iron yoke of the flux return is instrumented with four stations of muon detectors covering most of the 4π solid angle. Forward sampling calorimeters extend the pseudorapidity –Appendix A.1– coverage to high values, $|\eta| \leq 5$, assuring very good coverage. The overall dimensions of the CMS detector are a length of 21.6 m, a diameter of 14.6 m and a total weight of 12500 tonnes.

3.2.1 Inner tracking system

A particle emerging from the collision and traveling outwards firstly encounters the tracking system, which is made of silicon pixels and silicon strip detectors. It surrounds the interaction point, starting at 4.4 cm from the axis, has a length of 5.8 m and a diameter of 2.5 m. As it is the first layer of the detector it receives the highest intensity of particles, this is why the construction materials were chosen to resist radiation.

To measure the path without disturbing the particles trajectory, it only tracks its position in a few points. However, each measurement is accurate to 10 μm and hence those few pints are enough.

The tracker is designed to provide a precise measurement of the trajectories by charged particles (high-energy muons, electrons, charged hadrons, the decay of very short lived particles such as b-quarks, etc), such particles follow spiraling paths due to the homogeneous magnetic field of 3.8 T that is present over the full volume of the tracker. The curvature

of the paths of the particles reveal their momenta; the more curved the path is, the less momentum the particle has.

The tracking detector –Fig. 9– covers a pseudorapidity range of $|\eta| \geq 2.5$.

The energies of the particles are measured in the next layers of the detector, the calorimeters. Electrons, photons and jets (sprays of particles produced by quarks) will all be stopped by the calorimeters, allowing their energy to be measured. Both are explained in the next two sections.

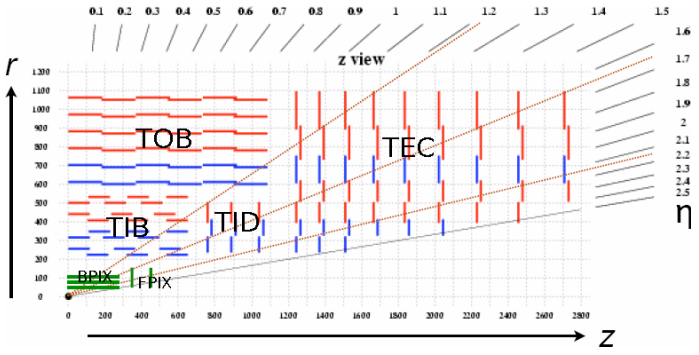

Figure 9: Schematic quadrant layout of the layers of silicon sensors in the CMS inner tracking system. Each line represent a module. Single sided modules (red), stereo modules (blue) and pixel modules (green) are grouped in the different tracker sub-systems. Tracker inner barrel (TIB), tracker outer barrel (TOB), tracker inner disk (TID), tracker endcap (TEC) are labeled on this quadrant representation [28].

3.2.2 Calorimeters

Electromagnetic calorimeter

The first calorimeter layer is designed to measure the energies of electrons and photons with great precision. Due to the electromagnetic interactions between particles, this layer is called electromagnetic calorimeter (ECAL): its purpose is to determine the energy of electrons, positrons and photons.

It is made of 6200 lead tungstate crystals mounted in the central barrel, enclosed by 7324 crystals in both endcaps and covering a pseudorapidity range of $|\eta| \geq 3.0$. Avalanche photodiodes and vacuum photomultiplier tubes are used as photodetectors in the barrel and in the endcaps, respectively.

The particles that interact by the strong force, hadrons, deposit most of their energy in the next layer, the hadronic calorimeter (HCAL), because they have a larger radiation length than the electrons or photons.

Hadronic calorimeter

The second calorimeter, the HCAL, aims to measure the energy of the hadronic jets and, due to the high coverage in η, the missing transverse energy of the neutrinos or other exotic particles. The HCAL –Fig. 10– has four main parts: the barrel (HB), endcap (HE), outer calorimeter (HO) and forward calorimeter (HF). The HB and HE sit behind the tracker and the electromagnetic calorimeter as seen from the interaction point, both are composed by plastic scintillators. The HB lies between the outer extent of the electromagnetic calorimeter (R = 1.77 m) and the inner extent of the magnet coil (R = 2.95 m). This radial restriction

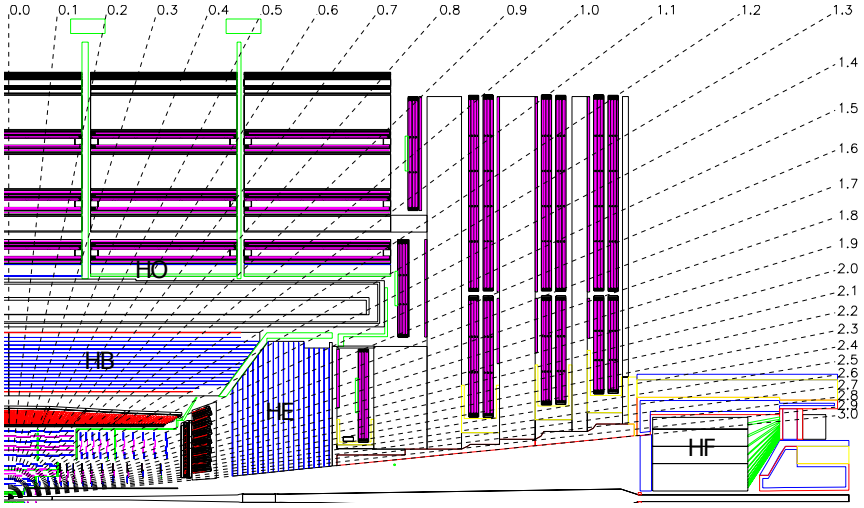

Figure 10: Layout of the CMS HCAL detector showing the locations of the hadron barrel (HB), endcap (HE), outer (HO) and forward (HF) calorimeters. The dashed lines are at fixed η values [28].

constrains the total amount of material which can be put in to absorb the hadronic shower. The HO is placed outside the solenoid, complementing the HB. For $|\eta| > 3.0$, the HF calorimeters placed at 11.2 m from the interaction point extend the pseudorapidity coverage to $|\eta| = 5.2$ using a technology based on Cherenkov radiation.

3.2.3 Muon system

The only particles known to penetrate beyond the HCAL and the magnet interact weakly, particles such as neutrinos and muons. Since the former ones are neutral and hardly interact at all they will escape the CMS, but the muon tracks are measured in the muon chamber –Fig. 11– detectors. For this reason, the muon chambers comprise the outermost layers of CMS, just after the solenoid. As charged particles, the trajectory of the muons is bent by the uniform magnetic field of 4T in the barrel region and by tracking their trajectories we can infer its momenta.

In barrel region are four stations made of drift tubes (DT) and resistive plate chambers (RPC) covering the volume inside $|\eta| < 1.2$. In the two endcap regions the muon rate levels and the background are high and the magnetic field is not uniform, here the cathode strip chambers (CSC) combined with the RPCs are used covering a pseudorapidity region of $|\eta| < 2.4$.

3.2.4 Trigger

Due to the amount of events, about one billion of proton proton interactions every second, that take place inside the CMS, a trigger system that can preselect potentially interesting events is needed. That is because is impossible to read out that much data and the most of it is not interesting for finding new physics.

The first level trigger (L1) and the High-Level Trigger (HLT) have a rate reduction capability designed to be at least a factor of 10^6.

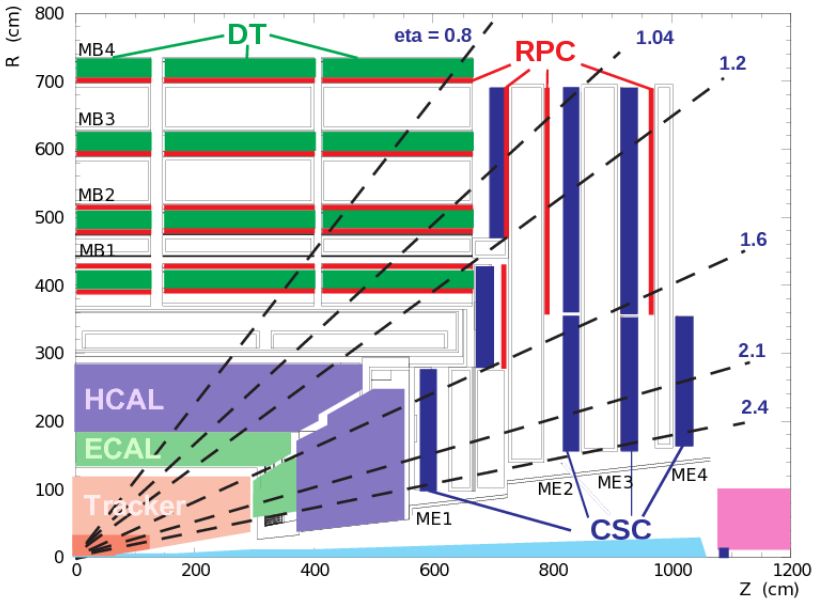

Figure 11: Layout of the CMS muon system detector showing the locations of the drift tubes (DT), strip chambers (CSC) and resistive plate chambers (RPC). The dashed lines are at fixed η values. [28]

Level 1 Trigger

The L1 trigger is implemented in hardware and it selects the best 10^5 events per second from the billion. It consists of an electronic system that uses coarsely segmented data from the calorimeters and the muon system, while holding the high-resolution data in pipelined memories in the front-end electronics. The L1 Muon Trigger analyses the hits from the muon system's CSC, DT and RPC. In each subsystem a local reconstruction is done and it determines from which bunch crossing the event is originated and it reconstructs a track segment with the number of muon stations containing hits and p_T-value. For the four muons with the best quality is determined the position, quality and p_T by means of the global trigger combining the information of the three mentioned subsystems. The muons pass the trigger depending on their p_T. The global trigger combines these four muons for triggers containing isolation.

HLT

The HLT is a software system implemented in a filter farm of about one thousand commercial processor.

This trigger has access to the complete read-out data and can therefore, assimilating and synchronizing the information of the different subdetectors, perform complex calculations similar to those made in the analysis off-line software if required for specially interesting events. So, after reconstructing the 10^5 events, the HLT select the 100 that are more prone to show something new about physics.

The HLT is subdivided in two levels named level 2 (L2) and level 3 (L3). On the former, a seed from the L1 trigger is taken for the reconstruction in the muon system with a precision of 15%. The decision in L2 is made based on the transverse momentum and some quality criteria. On the later, the L2 muon track is extrapolated and an additional track reconstruction is done on the tracker with a precision of 1% for not to high p_T.

Data distribution

After the trigger stage, the reconstructed data is stored on the offline system of the CMS. This data need to be stored, easily retrieved and analyzed by physicists all over the world. This requires massive storage facilities, global networking and immense computing power. CERN does not have the computing or financial resources to crunch all of the data on site, so in 2002 it turned to grid computing to share the burden with computer centers around the world. The result, the Worldwide LHC Computing Grid (WLCG), is a distributed computing infrastructure arranged in tiers, giving a community of over 10^4 users near real-time access to LHC data.

4 Analysis

In this section the analysis methodology for the search of new physics in the mono-μ channel with the proton-proton collision data recorded in 2015 at $\sqrt{s}$= 13 TeV is explained. A description of the data, background and signal is presented. Also the results and the exclusion limits are discussed.

This analysis is complicated because we have four particles in the final state of which only one can be detected. Since the signal is in general an ISR tagged search, other channels can explore the same signal with different final states. In Institute IIIA of the RWTH Aachen University the e+E_T^{miss} channel was used to study the DM signal and the decay of heavy gauge bosons into neutrinos [21].

4.1 Used data

The events used in this work correspond to the "/SingleMuon/Run2015D-16Dec2015-v1/MINAOD" data set. It was acquired in 2015 with a center of mass energy of $\sqrt{s}$ = 13 TeV (Run II). From the several data taking rounds of Run II, the used is run D which is characterized by proton proton collisions with a bunch spacing of 25 ns, a magnetic field of 3.8 T, total recorded luminosity of $\mathscr{L}$ = 2.30 ± 0.06 fb^{-1}, a total delivered luminosity of 2.38 ± 0.07 fb^{-1} and all the detector components working .

The single muon dataset used for the analysis corresponds to the latest reconstruction which was recalibrated the 16$^{\text{th}}$ December of 2015. The events in this channel have the following trigger requirements:

Trigger	Description
HLT_Mu45_eta2p1_v*	At least one muon with at least 45 GeV within $\|\eta\|$ <2.1
HLT_Mu50_eta2p1_v*	At least one muon with at least 50 GeV within $\|\eta\|$ <2.1
HLT_Mu50_v*	At least one muon with at least 50 GeV
HLT_IsoMu24_eta2p1_v*	At least one isolated muon with at least 24 GeV within $\|\eta\|$ <2.1

Table 1: Different high level triggers (HLT) used in the analysis.

The data is prepared in the MINIAOD version 2 format at CERN. This format represents a high level data tier for mainstream physics analyses featuring a small event size of 30-50 kb per event while retaining necessary event information [30]. For the analysis of the data samples, the events are converted into the PXLIO format, which is described in [31].

4.2 Monte Carlo Simulations

Many different MC samples are used in this analysis to simulate SM processes in order to determine the number of background events for this analysis and to simulate the various predicted DM signals. Since MC samples are produced with a number of events which normally do not match the integrated luminosity of the used collision data, the samples have to be weighted by a factor:

$$\omega = \frac{\sigma \mathcal{L}}{N_{MC}} \tag{4.1}$$

where σ is the full cross section used by the MC process, $\mathcal{L}$ is the luminosity of the used collision data and M_{MC} the number of generated MC events.

Cross sections of particle processes are calculated in expansion series of a QFT. Since there are an infinitive number of higher order corrections to each process like loops or vertex corrections, the calculation can only be performed to a certain level of accuracy. In almost all processes relevant for the LHC, the effect of the corrections decreases with rising order of the corrections. Some of the programs used to produce MC samples only consider cross sections without any higher order corrections. These cross sections are called "leading order" (LO) cross sections. Higher order corrections within the Standard Model can arise from electroweak or QCD processes where the QCD corrections are usually the dominant ones. Cross section calculation from diagrams containing one or two additional vertices are called "next-to leading order" (NLO) and "next-to-next-to leading order" (NNLO). The number of diagrams needed for one or two additional vertices depends on the process. These calculated higher order corrected cross sections are used to re-weight the MC samples which are produced at LO by applying a correction factor defined as $k = \frac{\sigma_{(N)NLO}}{\sigma_{LO}}$ to the scale factor from equation 4.1. [32]

4.3 Backgrounds

The processes whose final state is the same or can be mistaken with the signal are what is know as SM background contributions. It is fundamental to identify those processes and estimate accurately their relevance so that we can extract them from the data and hypothetical DM signal. A list of them can be found on the Table 2. For the estimation of the background data-driven does not work in this case because there are no symmetries that can be exploited. Therefore, the background modeling was done with Monte Carlo (MC) simulations.

The dominant background process –Fig. 12 (Left)– is $W \rightarrow \mu\nu$. This part of background is irreducible because its topology is almost the same as the one of the signal. The $W \rightarrow \tau\nu$ branch also contributes to the background, as the tau lepton is not stable and can decay to a muon and two neutrinos [33].

The $t\bar{t}$ and single t production process –Fig. 12 (Right)– is important, because the top quarks decay into a b quark and a W boson which may produce a single lepton, a potential second lepton could be outside the detector acceptance.

Also, the Drell-Yan processes (DY) ($Z/\gamma \rightarrow l\bar{l}$) can be confused with a lepton and E_T^{miss} if one of the two leptons is not identified or is outside the detector acceptance. If the lepton in the DY process is a τ, it can decay into μ, ν_τ and $\bar{\nu_\mu}$.

Two other processes are taken into account for the background prediction, but they are less relevant: The first of these processes is diboson productions (WW, WZ and ZZ), where one of the bosons decay into leptons and the other into quarks or neutrinos. The missidentification of the quarks may lead to a lepton and E_T^{miss} final state.

In Fig. 13 the backgrounds after applying the trigger selection and the kinematic cuts –Section 4.8– are shown in the E_T^{miss} spectrum. As described above, it can be seen that the dominant background process is the W boson decay, followed by the $t\bar{t}$ production.

The $t\bar{t}$, DY and diboson backgrounds were simulated at NLO and the W one at LO. For the higher order corrections of the SM W background the k-factors where calculated dependent on the invariant mass of the lepton and neutrino. The k-factors include the NLO electroweak correction as well as the NNLO QCD correction. The corrections can be combined either additive, eq. 4.2, or factorized, eq. 4.3. In this analysis, for the k-factor, the additive approach has been used. This approach assumes that the electroweak corrections except final state radiation (FSR) have an additive nature and the same correction

Process	Generator	Subsample	cross section (pb)	Generator order
$W \to \mu\nu$	PYTHIA		9.13×10^3	LO
$W \to \mu\nu$	PYTHIA	$500 > p_T < 100$	1.46	LO
$W \to \mu\nu$	PYTHIA	$p_T > 500$	1.53×10^{-3}	LO
$W \to \tau\nu$	PYTHIA		9.13×10^3	LO
$W \to \tau\nu$	PYTHIA	$500 > p_T < 100$	1.46	LO
$W \to \tau\nu$	PYTHIA	$p_T > 500$	1.53×10^{-3}	NLO
$Z \to \mu\mu$	POWHEG	$m_{\mu\mu} > 20$	1.87×10^3	NLO
$Z \to \mu\mu$	POWHEG	$m_{\mu\mu} > 120$	1.19×10^1	NLO
$Z \to \mu\mu$	POWHEG	$m_{\mu\mu} > 200$	1.49	NLO
$Z \to \mu\mu$	POWHEG	$m_{\mu\mu} > 400$	1.09×10^{-1}	NLO
$Z \to \mu\mu$	POWHEG	$m_{\mu\mu} > 500$	4.42×10^{-2}	NLO
$Z \to \mu\mu$	POWHEG	$m_{\mu\mu} > 700$	1.02×10^{-2}	NLO
$Z \to \mu\mu$	POWHEG	$m_{\mu\mu} > 800$	5.49×10^{-3}	NLO
$Z \to \mu\mu$	POWHEG	$m_{\mu\mu} > 1000$	1.80×10^{-3}	NLO
$Z \to \mu\mu$	POWHEG	$m_{\mu\mu} > 1500$	1.71×10^{-4}	NLO
$Z \to \mu\mu$	POWHEG	$m_{\mu\mu} > 2000$	2.21×10^{-5}	NLO
$Z \to \tau\tau$	PYTHIA	$m_{\tau\tau} > 20$	1.53×10^3	LO
$Z \to \tau\tau$	PYTHIA	$200 > m_{\tau\tau} > 100$	3.49×10^1	LO
$Z \to \tau\tau$	PYTHIA	$400 > m_{\tau\tau} > 200$	1.18	LO
$Z \to \tau\tau$	PYTHIA	$800 > m_{\tau\tau} > 400$	8.70×10^{-2}	LO
$Z \to \tau\tau$	PYTHIA	$m_{\tau\tau} > 800$	4.50×10^{-3}	LO
$t\bar{t}$	MC@NLO		2.11×10^2	NLO
$t \to bl\nu$ (s-Chanel)	POWHEG		2.82	NLO
$t \to bl\nu$ (t-Chanel)	POWHEG		4.70×10^1	NLO
$t \to bl\nu$ (tW-Chanel)	POWHEG		1.07×10^1	NLO
$t \to bl\nu$ (s-Chanel)	POWHEG		1.57	NLO

Table 2: List of backgrounds with their generators used for simulation and their cross sections at leading order (LO) or next-to leading order (NLO). The cross sections are provided as calculated by the generator (LO for PYTHIA and MADGRAPH , NLO for POWHEG and MC@NLO), the influence of higher order corrections is described by a K-factor. The generator constrains in the column Subsample are in GeV.

needs to be added for all orders of QCD corrections. For the calculation of the systematic uncertainties on the k-factor is used the factorized approach, which assumes that the higher order electroweak are the same for all the orders of QCD [34] . The differential cross sections for an observable, $\mathcal{O}$, for both approach are:

$$\left[\frac{d\sigma}{d\mathcal{O}}\right]_{QCD\oplus EW} = \left[\frac{d\sigma}{d\mathcal{O}}\right]_{QCD} + \left[\frac{d\sigma}{d\mathcal{O}}\right]_{EW} - \left[\frac{d\sigma}{d\mathcal{O}}\right]_{LO} \tag{4.2}$$

$$\left[\frac{d\sigma}{d\mathcal{O}}\right]_{QCD\otimes EW} = \left(\frac{\left[\frac{d\sigma}{d\mathcal{O}}\right]_{QCD}}{\left[\frac{d\sigma}{d\mathcal{O}}\right]_{LO}}\right) \times \left[\frac{d\sigma}{d\mathcal{O}}\right]_{EW} \tag{4.3}$$

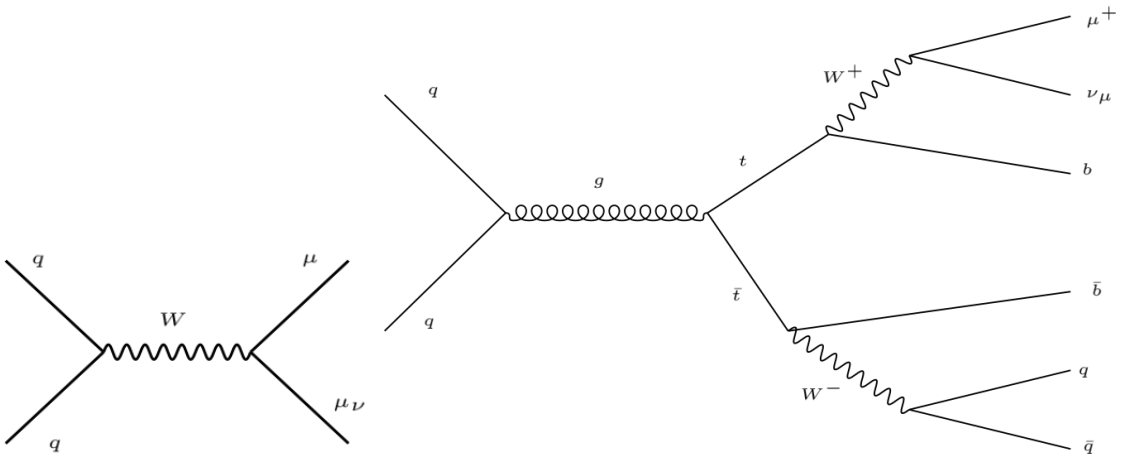

Figure 12: Feynman diagrams for background processes. Left: $W \to \mu\nu$. Right: $t\bar{t}$ production.

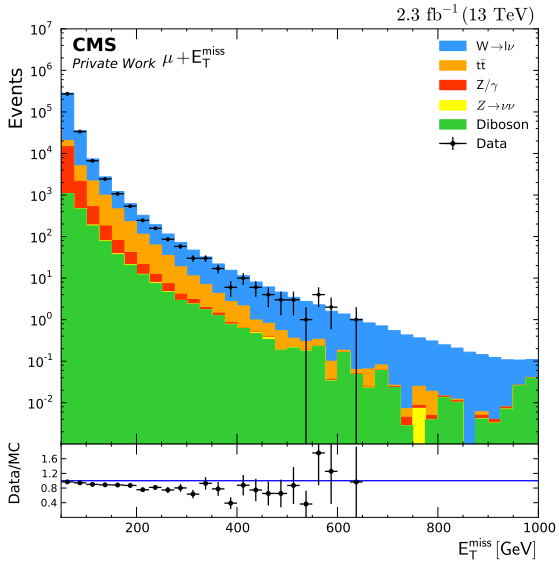

Figure 13: E_T^{miss} distribution for the background and the data after aplying the trigger and the kinematic cuts.

4.4 Missing transverse energy and mass

The DM particles and the neutrino leave the detector unmeasured. The Z component (beam direction) of the momentum is unknown and therefore cannot be used for the analysis, but what is known is that, before the collision, the momentum and the energy in the transverse plane is zero. By the conservation of the momentum, the transverse momentum of the reconstructed particles[5,6] ($\overrightarrow{p}_T$), in this case only the muons, should be compensated by the non-detected ($\overrightarrow{p}_T^{miss}$). The $\overrightarrow{p}_T^{miss}$ is the total momentum of all the particles that are not detected and is defined, by $\overrightarrow{p}$ conservation, like $\overrightarrow{p}_T^{miss} = -\sum \overrightarrow{p}_T$.

The missing transverse energy (E_T^{miss}) is the parameter used for the identification of the DM. It is the imbalance of the total transverse momentum in the event and hence it is reconstructed from the $\overrightarrow{p}_T$; $E_T^{miss} = |\overrightarrow{p}_T^{miss}|$.

In this thesis is analyzed the distribution concerning the transverse mass (M_T) instead of the E_T^{miss}. The M_T is defined as:

$$M_T = \sqrt{2 \cdot E_T^{miss} p_T \cdot (1 - cos[\Delta\phi(l, \overrightarrow{p}_T^{miss})])} \tag{4.4}$$

Where the $\Delta\phi$ is defined as the angle between the directions of p_T^{miss} and $E_T = |\vec{p_l}|$.

The motivation to use the M_T distribution instead the E_T^{miss} is that in with the transverse mass the separation between the signal and the background is more evident than with the missing transverse energy.

4.5 Muon reconstruction

To have a good reconstruction of the muon is fundamental in this analysis because it is the only object that can be measured in the detector and, since we rely on the simulation for the main W background, the reconstruction is discussed here.

As described in section 3.2, muons can be measured in the inner tracking system and the muon system. This particle is identified by its presence in the muon system, as it is the only SM particle that can reach this part of the detector.

Muon energy is not determined by calorimeters because it is a minimum ionizing particle, which means that it have a very low mean energy loss rate through matter. Therefore, we have to determine the muons[7] energy from the bending of its trajectory. The momentum, p, of a charged particle can be derived from the bending radius in a magnetic field, r,by equaling the force done by the magnetic field, B, to the centripetal force:

$$m\frac{v^2}{m} = vqB \tag{4.5}$$

$$p_T = rqB \tag{4.6}$$

Where q is the charge. The r is determined from the sagitta (distance –Fig. 14– from the center of the arc to the center of its base), s, and the arc length, l, as follows:

$$r^2 = (l/2)^2 + (r - s)^2 \tag{4.7}$$

$$r = \frac{(l/2)^2 + s^2}{2s} \tag{4.8}$$

[5] $p_T = p \cdot sin\theta$

[6] The way $\overrightarrow{p}_T$ is measured is explained in section 4.5.

[7] Sagitta method is also used for other charged particles.

and if $s << r$

$$r \approx \frac{l^2}{8s} \tag{4.9}$$

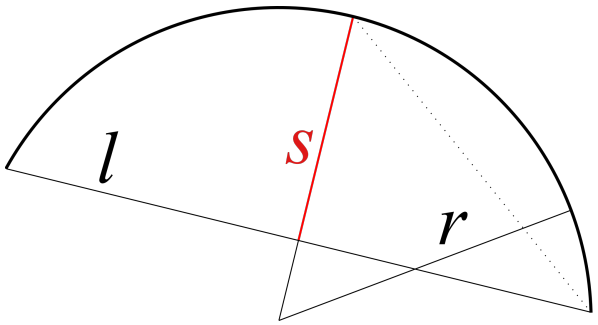

Figure 14: The arc represents the path of the particle. With the sagitta and the arc length, the radius of curvature can be determined [35].

The main uncertainty on this measurement is the uncertainty on the sagitta and it can be modeled with a Gaussian distribution [36].

The reconstruction of muons with high momentum is difficult because the curvature is small and hence the sagitta also becomes minute. When s is approximately below 20 μm it is hard to be measured. For instance, for a B= 3.8 T, a muon with p_T = 500 GeV has a s = 0.4 cm and one with[8] p_T = 1 TeV has s = 0.2 cm. Extrapolating, for a $p_T \approx$ 10 TeV s = 20 μm. Furthermore, the electromagnetic shower plays a role if the energy is above 900 GeV, critical energy when the μ start the shower.

The trajectories are measured independently in the tracker and in the muon system. Due to the high occupancy, tracks are seeded in the tracker iteratively from the pixel detector. With a track building method and Kalman filters, the trajectories are reconstructed, taking into account the effects of the material and changes in the magnetic field. In the muon system trajectories are based on segments, which are like tracks in a single muon chamber. At least two segments are necessary to reconstruct a track in the muon system. At this point, two different algorithms are used for the reconstruction: "the global muon" and the "tracker muon" approach. The first one matches a track from the tracker system to each track of the muon system and a common trajectory is found using a Kalman filter [37]. In the "tracker muon" approach, the tracks in the tracker with $p > 2.5$ GeV and $p_T > 0.5$ GeV are are propagated to the muon system and, if at least one matching segment exists, a tracker muon is declared. For high p_T muons the radiation has to be taken into account. Therefore delicate high p_T refits, which anticipate showering muons, are done. From the different refits the one with the best fit quality is chosen. These methods are then used in the so called "particle flow algorithm", which builds particle candidates from every measurement in the detector and combines different detector components with each other.

4.6 Muon selection

From all the reconstructed muons that were selected after the trigger filtering, a subset was chosen based on different criteria that ensure that the reconstructed particles are muons from the primary vertex of the collision with momenta that we can determine accurately. In addition, further criteria have been chosen so that the number of background events is reduced without diminishing the number of signal events.

[8]For high p_T it is considered that l = 4 m, which is the usual turning point in CMS.

4.6.1 Event selection

These criteria are used to make sure that what we are detecting is a primary muon with a well defined momentum. Candidate events with at least one high-p_T muon are selected using single-muon trigger (with $p_T > 45$ GeV).

The reconstruction of muons is made with the information from the tracker and the muon system together and is optimized for high transverse momenta. Each muon is required to have:

- At least one hit in the pixel detector.
- At least six tracker layer hits.
- Segments in two or more muon detector layers.
- A transverse impact parameter, $|d_0|$, of less than 0.02 cm and to have a longitudinal distance parameter, $|d_z|$, of less than 5.5 cm. This significantly reduces the amount of hadronic punch-through.
- The relative p_T uncertainty has to be less than 30%; this ensures a well reconstructed muon.
- $|\eta| < 2.1$ to match the trigger acceptance.
- Muon isolation requires that the scalar sum of all tracks originated from the interaction vertex within the $\Delta R = \sqrt{(\Delta\phi)^2 + (\Delta\eta)^2} > 0.3$ cone around its direction is less than 10% of the muons p_T, excluding the muon itself.
- If there is a second muon with $p_T > 25$ GeV, the event is vetoed to reduce the Drell-Yan and cosmic ray backgrounds.

If any of these conditions are not fulfilled, the muon is rejected. [20]

4.7 Signal generation

Unless stated otherwise, this section is based on [20].

The signals corresponding to the different DM models are computationally simulated for the analysis together with the data from CMS and the background. Then is tested if they are compatible with the existence of the DM as described in the simplified models.

Depending on the coupling mechanism, different MC generators are used to generate the signal. Considering the AV[9]coupling mediator is used Madgraph 5. For the S and P coupling mediators is used the JHU generator, which generates a single-produced X resonance that in this case is the mediator particle. With the external tool `boltdmec`, the DM decay of the mediator is simulated. This tool is chained to the output of the JHU generator.

All generated signal events, independent of the model, are processed through a full simulation of the CMS detector based on GEANT4, a trigger emulation and the event reconstruction chain. The leptonic decay of this boson complements the established mono-jet and mono-γ searches and has two major advantages: a lower SM background and a lepton to trigger the event. The events are reconstructed with two-body decay kinematics.

[9]Also for the V but is not discussed.

M_{med} (GeV)	M_χ (GeV)							
	1	10	20	50	100	150	500	1000
10	A, P	A		A				
20	A, P		P					
50	A, P	A,P		A				
100	P	A, P		S, P	A			
195					A			
200	A, P	A,P		A, P	P	A		
295						A		
300	P	A, P		A, P	A, P	P		
500	A, P	A, P		A, P	A,P	A, P		
995							A	
1000	A, P, S	A, P, S		P, S	A, P, S	A, P, S	P	
2000	P	P, S		A	A, P	A, P	A, P	P
10000	A, P, S	A, P, S		A, P, S	A, P, S	A, P, S	A, P, S	A, P, S

Table 3: Generated parameter points. Available generated mass points for leptonic W decay samples (exception: the sacalar coupling lised are leptonic + hadronic decays). The notation A, S, P means hat the samples are availabe with axial vector, scalar and pseudoscalar coupling.

4.7.1 Model parameters selection

Values for the model parameters –Section 2.3.3– had to be chosen for the GEANT4 simulation. As this process is computationally expensive, the subset[10] of simulated signals should include a parameter selection which dominantly affects the resulting exclusion limits, this changes the shape of the M_T distribution. The mediator strength couplings (g_{SM} and g_{DM}) were fixed to 1, and for the mediator width, we used two values: $\Gamma = \frac{M_{med}}{8\pi}$ and $\Gamma = \frac{M_{med}}{3}$. The other relevant parameters for the signals generation are the DM and mediator masses. Then, from the generated parameter points –Table 3– that are produced with the full detector simulation, we study the effects of the variation of those M_{med} and M_χ and which give us the most significant differences. Those will be the ones we use for the analysis.

In order to test the influence of the masses of the DM particles and the mediator boson, we compare the M_T distribution of different DM signals for each model.

The first model to analyze is the AV. To test the dependence on a parameter we fix the others and modify the one in which we are interested in so that the variations can be studied. For the signal plots displayed below, a fixed binning of 100 GeV has been used. On the Fig. 15 (left) the impact of the DM mass is exterminated by plotting a range of different M_{DM} (1, 10, 50 and 150 GeV) for a constant M_{med} of 200 GeV. As can be seen, all the lines overlap for low values of M_T. For higher M_T, the signals stop overlying and they present a linear behavior with slopes that are not sorted by M_χ. Nevertheless, the slope of the off-shell[11] signal is flatter. On the right figure, the mediator mass dependence is tested. In contrast to the left figure, in this case the signals are more similar and it seems that the influence of the M_{med} is not significant. There is neither a considerable difference between on-shell and off-shell signals.

[10] Each subset is identified by g_{SM}, g_{DM}, M_{med} and M_χ

[11] Virtual particles are produced off-shell because they do not satisfy energy-momentum relationship. In this case, off-shell: $M_{med} < 2M_\chi$

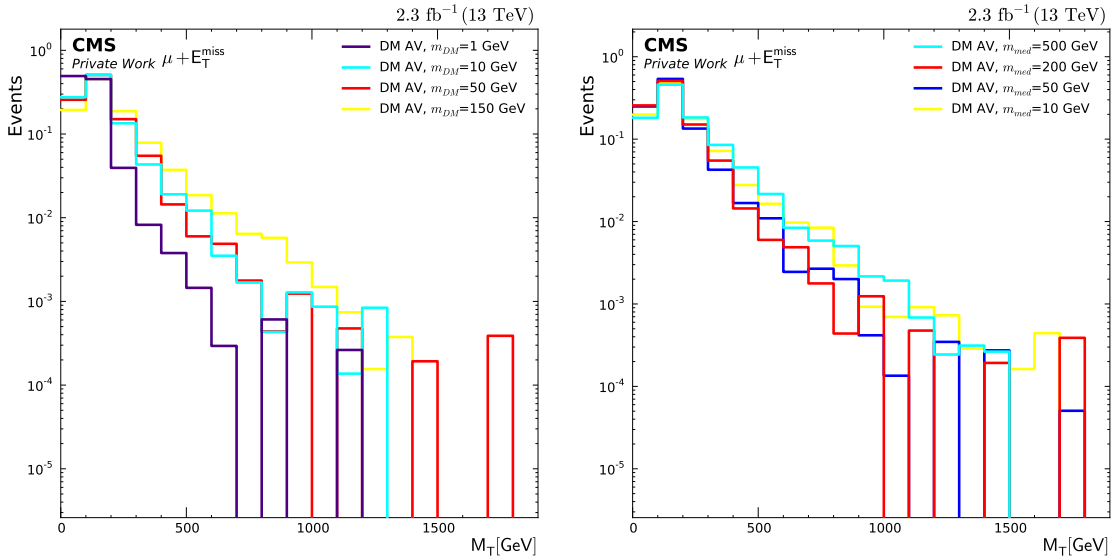

Figure 15: M_T distribtions of DM signals for the AV model. Left: M_χ dependece studied with M_{med}= 200 GeV. Right: M_{med} dependence studied with M_χ= 50 GeV.

Is important to mention that the M_χ influence is not simulated for the S and P models, the implementation of JHU generator does not consider M_χ. For these two modes, the mediator width play an important role. In Fig. 16 can be seen that the mediator width for $M_{med} > 500$ GeV it changes abruptly for the scalar and pseudoscalar coupling mediator due to the Γ_{WW} component. Therefore, the simulation is not accurate for mediator masses above half TeV and the region in which one would prefer to work is between $M_W/5$ and $5M_W$ (approximately between 20 and 400 GeV).

For the S model there is only one generated parameter point inside this rang, the rest have mediator masses above 1 TeV. In Fig. 17 (Left), the overlap between the two signals corresponding to M_{med}= 1 TeV confirm that the M_χ in not considered for the simulation. The three signals with mediator masses above 500 GeV have the same shape and are considerably higher than the other one. On the other hand, for the P model a larger set of parameters was available. In Fig. 17 (Right) can be verified again that, as expected, the DM mass has no effect over the signal. The M_χ = 10, 50 and 100 GeV overlap for a fixed mediator mass of 200 GeV, even the one off-shell does. For the three different M_{med} showed for the P model can be observed that the signals have the same shape and that the higher the M_{med} is, the larger is the signal.

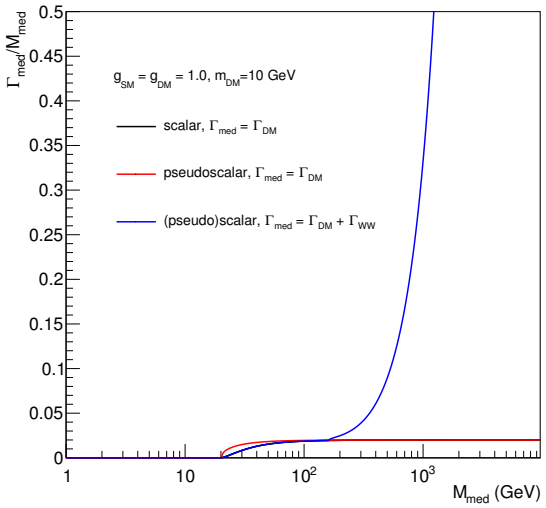

Figure 16: Γ_{med}/M_{med} for a scalar and pseudoscalar coupling mediator which couples to a pair of W bosons and DM. In order to visualize the influence of the W boson pair coupling contribution, the ratio corresponding to DM coupling only is shown as well. [21]

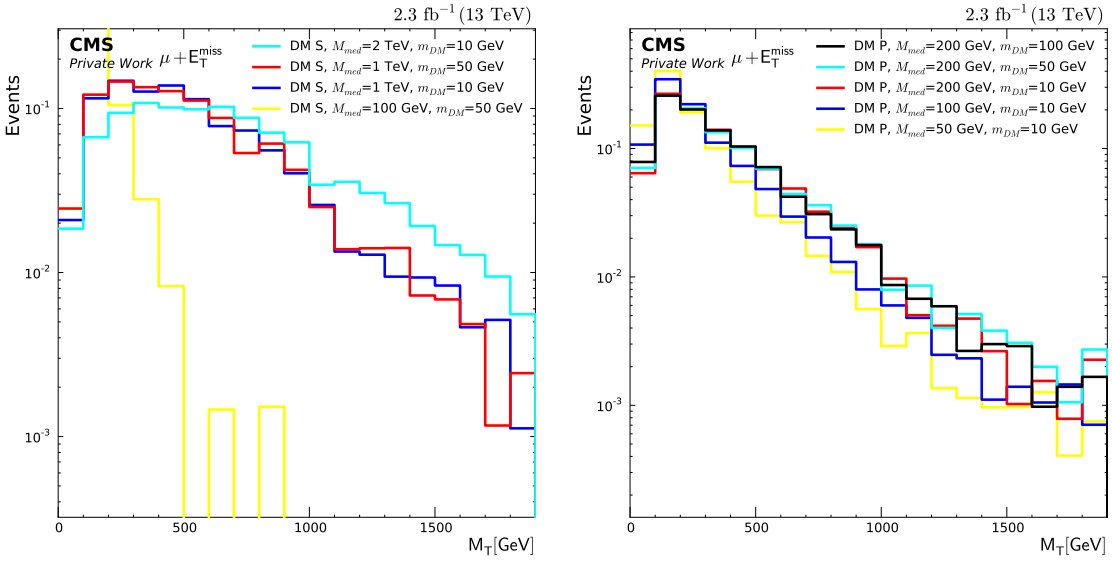

Figure 17: M_T distributions of DM signals. Left: Scalar model. Despite it was stated that the range of masses for the sacalar model to be analyzed had to be below 500 GeV only Right: Pseudoscalar model.

4.8 Kinematic selection

The kinematic selection aims to ensure a better signal to background ratio. For this purpose, the ranges (in the $\Delta\Phi$ and E_T^{miss} distributions) where the background is not large compared to the signal, are kept. This means, that only the regions where the signal is more likely to be detected[12] are considered for the analysis. Because of the conservation of momentum, the selection of a balanced back to back event ensures the correct reconstruction of the event. As it has been done in previous similar analysis; two kinematic cuts are applied in order to suppress the background noise with respect to the signal:

- The ratio of the muon transverse momentum and the missing E_T must lie in the region

$$0.4 < p_T/E_T^{miss} < 1.5 \tag{4.10}$$

  This ensures the back-to-back pattern between the lepton and the undetected particles. In Fig. 18 (Left) the signal and background are represented d in the p_T/E_T^{miss} spectrum. The ranges where the background is not much higher than the signal are the non-excluded by the p_T/E_T^{miss} kinematic cut. The peak of the aground on the left figure is due to the SM W boson production. It can be noticed that the signal to background ratio for p_T/E_T^{miss} below 0.5 GeV is good and, nevertheless, is excluded. This is because the cuts are optimized for high M_T and in this plots only the low M_T is visible. There is also a steeply falling flank, where a small shift in the ratio can easily create an offset. The construction of this type of plots is described in the next section.

- For the same reason, the azimuthal angle is constrained to:

$$|\Delta\phi(\mu, E_T^{miss})| > 2.5 \text{ rad} \tag{4.11}$$

  Fig. 18 (Right) shows the signal and background before and after applying the $\Delta\Phi$ cut. As can be seen, the part of the $\Delta\Phi$ spectrum that is below 2.5 rad has much more background than signal and therefore that range is removed from the analysis. This suppression put away about the three fourths of the background while only the half of the signal was removed. What remains has much greater signal to background ratio.

[12] The signal only can be detected when the background is not much more hihger.

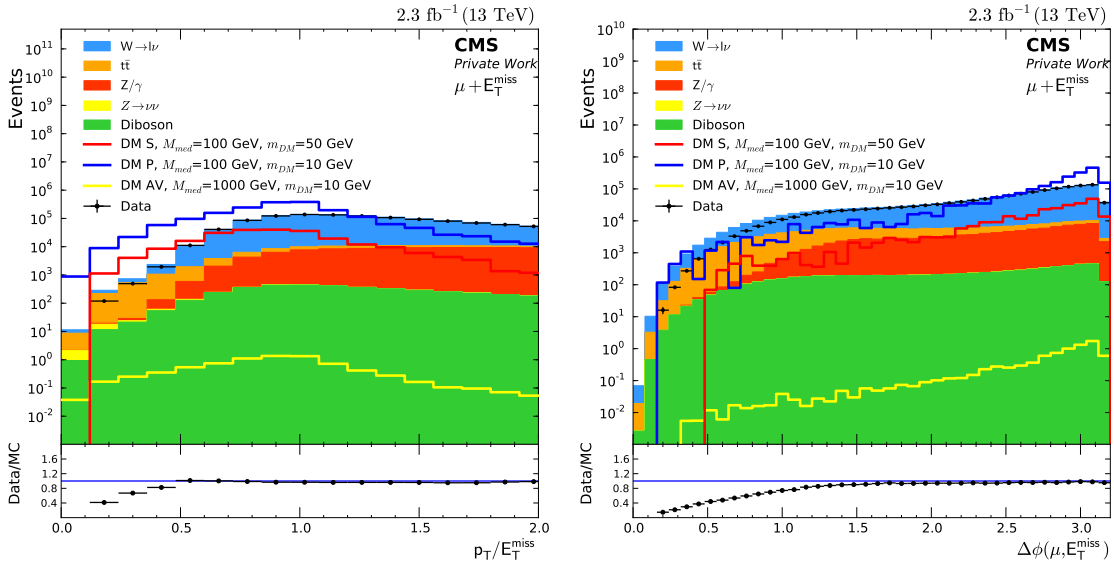

Figure 18: Left: p_T/E_T^{miss} distribution with $\Delta\Phi$ requirement. Right: $\Delta\Phi$ distribution with p_T/E_T^{miss} requirement.

4.9 Final M_T distribution

In the Fig. 19 the transverse mass distribution of the background, data and DM signals for the AV, S and P models is shown. Apart from the muon trigger selection and the kinematic cuts described in Section 4.6, additional cuts are applied in order to improve the signal efficency[13]and significance[14]: a lower bound on transverse mass $M_T > 50$ GeV and an offline p_T requirement of $p_T > 30$ GeV. The colored areas represent the stacked background, as expected –Section 4.3– the dominant one is the W background. The colored lines correspond to DM signals and the dots to Run II data. The signals are not taken into account to plot the background area, *i. e.* they are not stacked. A logarithmic binning has been used so that the bins get wider as the M_T increases. The distribution is divided in 50 bins from 100 GeV to 2000 GeV equally spaced in $logM_T$. The error bar of the dots represents the statistical uncertainties on the data. The shaded area stands for the systematic errors of the background.

In the left plot of Fig. 19 the M_T distribution is presented. In this plot the three on-shell signals correspond to the different models with a $M_{med} = 100$ GeV. The P coupling model present more events than the S and this one more than the AV but for other model parameter selection the slope of the distribution could change as can be seen in figures 17 and 15.The AV and S coupling models present a total reduction on the number of events after 850 and 900 GeV respectively. The presence of DM would be identified by an excess of the data respect to the SM predictions in the M_T distribution. If this excess is similar to the value of the DM signals in that specific region of the distribution, then we have an indication of DM particle [15]. In this case, no significant difference between the data and the MC simulations has been found, *i.e.* that we have an agreement with the SM predictions, and therefore no DM particle has been found (specially at low M_T values).

[13]Ratio of the number of events after and prior application of a certain cut.

[14]Defined as $\frac{N_{sig}}{\sqrt{N_{sig}+N_{bg}}}$ where N_i is the number of signal and background eventes in a bin.

[15]A great excess in data with respect to SM predictions would imply a finding but not necessarily DM.

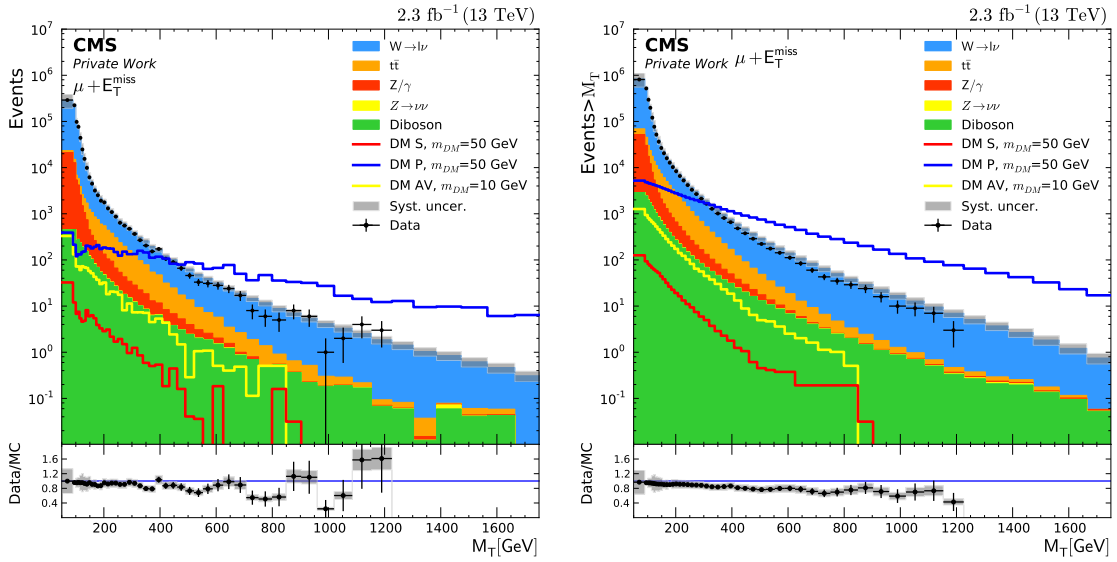

Figure 19: M_T distribution of DM signals examples for the three simplified models with M_{med} = 100 GeV including the data and the background after the muon trigger and the after all applied cuts. The cross sections are calculated for the narrow width approach, $\Gamma = \frac{M_{med}}{8\pi}$. The filled areas show the stacked background distributions while the signals are drawn as solid lines. Left: Final M_T distribution. Right: Cumulative M_T distribution.

In the right plot of Fig. 19 the cumulative M_T distribution is displayed. It is constructed by:

$$N(M_T) = \sum_{x=M_T}^{\infty} N(x) \tag{4.12}$$

It can be noticed that for $M_T > 200$ GeV there is deficit of data with respect to the MC simulations. In the simple distribution (left plot) this lack of data is not general, actually there is an excess of data at some points of the M_T distribution. The maximum observed transverse mass –Appendix A.2– is 1200 GeV.

These results can be compared with the obtained for $\sqrt{s}$=8 TeV analysis, which only considered the AV and V models. In Fig. 20 there is a slight excess of data events compared to the standard model expectation starting from about 600 GeV. The maximum observed transverse mass is 2.1 TeV. In contrast to our outputs, the 8 TeV plot shows more data than simulated events. This imbalance is more favorable to the existence of new physics but its significance, 2.6σ at most, is not enough to claim a discovery.

In the field of DM searches, a similar analysis is been done for the electron channel. In Fig. 21 the M_T distribution of the data and background for the e + E^T_{miss} is shown to be compared with the reconstructed DM signal. The distribution has been done after applying the electron trigger[16], the kinematic cuts and a lower mass bound of $M_T > 50$ GeV and an offline p_T cut of 130 GeV.

The M_T distribution shows an overall agreement between data and simulation, this coincidence with the SM predictions means that no evidence of new physics has been found and hence exclusion limits on the physic model parameters had to be derived.

[16] `HLT_Ele115_CaloIdVT_GsfTrkIdT_v*`

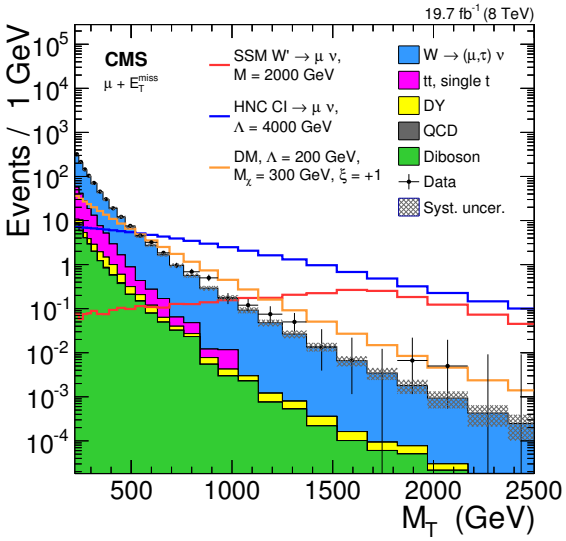

Figure 20: Invariant mass distribution for the muon channel corresponding to $\sqrt{s}$= 8TeV. The uncertainty on the total number of expected background events is displayed as a shaded bar. [38]

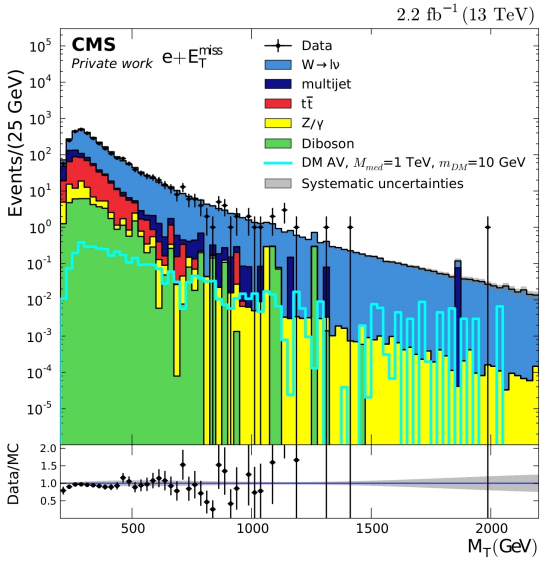

Figure 21: Invariant mass distribution for the electron channel corresponding to $\sqrt{s}$= 13 TeV. The signal for AV model with M_{med} = 1 TeV and M_{χ}= 10 GeV is displayed [21].

4.10 Systematic uncertainties

Different sources of systematic uncertainties –Fig. 22– are considered in the analysis. These uncertainties for the number of expected events may affect the shape and overall normalization of the M_T distribution for both: the signal and the background. They are classified in global (*e.g.* luminosity, pile up rewriting) or object-related (*e.g.* energy scale and resolution on the muon identification) uncertainties. For each source of uncertainty, its upper and lower values are propagated to the objects' kinematics, the resulting distributions are recalculated and the kinematic selection reapplied. The difference in the M_T distributions with respect to the nominal one is taken as the systematic uncertainty from that source [39].

One of the main sources of systematic uncertainties is the potential missmeasurement of the muon p_T, which may come from the detector resolution or systematic distortion on the scale calibration which affects the M_T, smearing it. Fig. 22 shows the influence of the uncertainties on the background prediction as a function of M_T. The dominant uncertainty comes from a possible bias on the transverse momentum scale, at very high p_T values, which may arise from an imperfect modeling of the alignment in the tracker or the muon systems. At lower M_T the dominant uncertainty is the resolution. Below a description of some relevant uncertainties is shown:

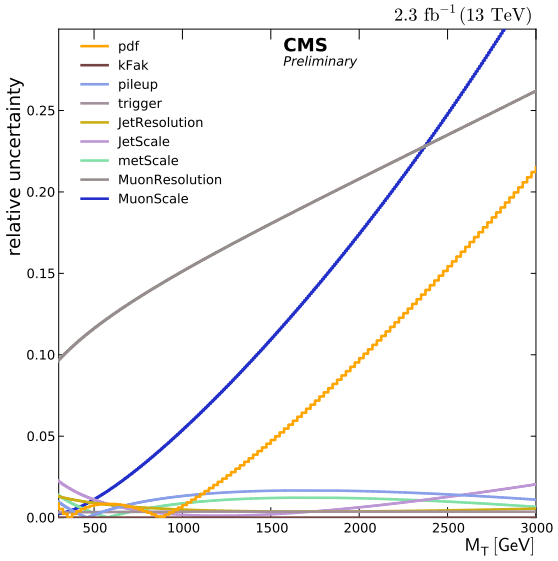

Figure 22: Effect of the systematic uncertainties on the number of background events as a function of M_T.

Reconstruction efficency

Only small deviations to the output of the actual detector are expected. In order to match the Monte Carlo efficiency to the data efficiency, a scale factor is determined. To find out this parameter, first the efficiencies are estimated using the tag-and-probe method. The tag-and-probe procedure consists on studying the decay of a Z boson into two muons. The lepton that satisfies the tight quality muon selection criteria – Section 4.6– is declared the tag lepton. The other lepton, the probe one, is independently tested. [40]

Muon scale

The muon scale is determined with the end-point method using cosmic muons. This procedure is based on the assumption that the rate of muons asymptotically approaches to zero for high energies [38]. The scale factor had to be fixed using the 2D graphs[17] created from the scripts CIEMAT CMS group scripts [18] that were provided by Alberto Escalante del Valle.

Muons resolution

The muon revolution is refereed to the quality of the measurement of the muon p_T. The higher the p_T is, the less is the bending of the muon trajectory and, therefore, the worst is the resolution. This uncertainty, as well as the muon scale, can be determined using cosmic muons by comparing the upper and lower halves of the detector. Only central cosmic muons can be used to measure this uncertainty [38].

Luminosity

This uncertainty affects the entire M_T distribution as a whole. It is measured using the pixel detector and calibrated by Van-der-Meer scans [41]. The uncertainty in the total integrated luminosity is 2.7% [39]

Missing transverse energy

The different uncertainties are directly translated into the determination of the E_T^{miss}, which is measured with the particle flow algorithm . The systematic sources affecting the E_T^{miss} are the muon p_T, the p_T of the reconstructed jets and the energy of the unclustered objects. The muon scale and resolution uncertainty are taken into account for both; the muon itself and the E_T^{miss}.

Pile-up

The pile-up refers to the number of additional interactions in the same bunch crossing, which increases the number of vertices in a given event. The effect is taken into account in the simulations by superimposing minimum bias interactions to provide the same conditions. [42]

K-factor

The application of k-factors, introduced in section 4.3, is accounting for higher order corrections. This factor is the result of dividing bin-by-bin the cross section values of the NLO and the NNLO in the distribution of W generated masses. The uncertainty on this factor is the 5% plus the difference with the differential cross section for the factorized approach [39]. The value of the k-factor is 1.2 for M_T arround the W peak and it decreases untill 0.8 for high transverse masses.

[17] Slide 38 `https://indico.cern.ch/event/516188/contributions/2039530/attachments/1252319/1847050/MuonScale_updatedV2.pdf`

[18] https://github.com/aescalante/ExampleScaleHighPt/blob/master/include/GeneralizedEndpoint.cc

Parton distribution functions

The Parton model is a way to analyze high-energy hadron collisions that was proposed by Richard Feynman in 1969 [43]. These functions (PDF) are used to describe the probability for the type and momentum fraction of a single parton (*e.g.* a hadron) in the simulation of hadron collisions. They are determined, among others, from deep inelastic experiments. The PDF uncertainty for the background has been estimated using the official LHC Run II recipe from the LHC4PDF group. Where a meta pdf set is build, which envelops all pdf sets, which are relevant for the LHC, and their uncertainties. The PDF sed used in this analysis is PDF4LHC15_nlo_30_pdfas [44].

4.11 Exclusion limits

When no significant discrepancy between the data and the SM predictions has been found, we can exclude certain ranges of values for the model parameters of the analyzed models. The deviations of data from the SM background on the transverse mass distribution are used with this purpose. A theoretical signal cross section limit is derived from NNLO calculations and with it we can exclude a range of values of the different parameters of the parameter space. More specifically, the M_χ and M_{med} are the limited parameters. The exclusion limits are determined with 95% of confidence level (CL). The observed limits are calculated with the data and the expected limits are created using the background as if it was the data. In order to claim a discovery of an unusual phenomenon, a deviation more significant than 5σ (99.99994% CL) must be observed, if the deviation is of 3σ (99.73% CL) there is an evidence.

4.11.1 Limits in one dimension

In the one dimensional limit plot, the cross section is plotted for a fixed dark matter mass and a variable mediator mass (M_χ = fix., M_{med} = x-axis). In these plots the theoretical, observed and expected cross sections are represented. The $\pm1\sigma$ (68% CL) and $\pm2\sigma$ (95% CL) intervals, shown in green and yellow color bands respectively, are the 68% and 95% two sided intervals from the expected limits spread with the systematic and statistical uncertainties. The expected value dashed line is the mean of the previous intervals. These limits have been calculated using the asymptotic analysis method which is described in the references [45] and [46].

The plots were generated for M_χ = 1, 10, 50, 100, 150, 500 and 1000 GeV. In the figures 23 and 24 limit plots for the AV, S and P models are shown for different M_χ. The red line corresponds to the conservative upper bound, $\Gamma = \frac{M_{med}}{3}$, and the blue one to the narrow width approach, $\Gamma = \frac{M_{med}}{8\pi}$. As explained in section 2.3.3, while the narrow mediator width corresponds to the eq 2.3 considering only one quark type and one color, the conservative width comes form considering the six quark flavours and three colors in the same equation.

We exclude theoretical cross sections (red and blue ones) above the observed cross section because this means to have a greater cross section and this implies being more detectable. Therefore, in the range of M_{med} where $\sigma_{theory} > \sigma_{observed}$ (for a fixed model and M_χ) the mediator mass can be excluded from the model. The same happens with the $\sigma_{expected}$ instead the observed, therefore we have two different ranges of exclusion; the expected and the observed. For instance, in Fig. 23 left, can be seen that for the upper bound the masses below 400 GeV are excluded for the AV mediator model for a M_χ= 1 GeV. The same procedure of exclusion is done for figures 23 right (only the narrow width, in which M_χ between 90 and 120 GeV are excluded) and 24. In the case of Fig. 23 right (only conservative width) there

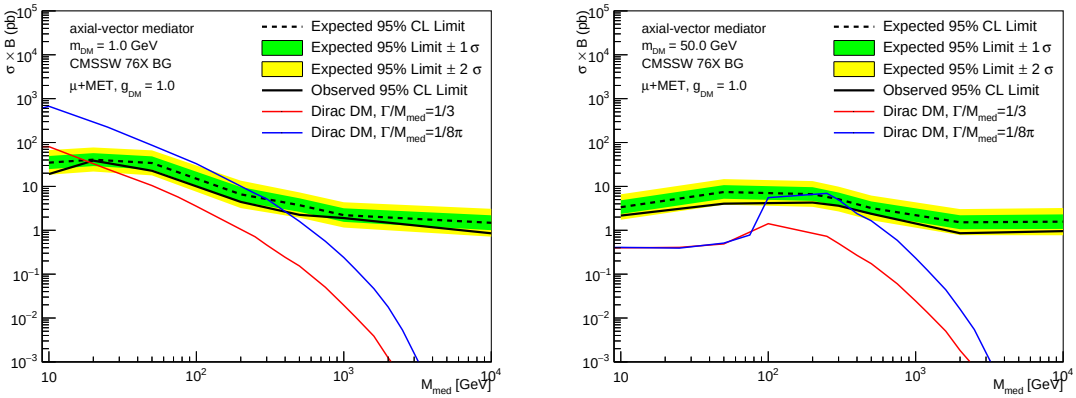

Figure 23: M_{med}-dependent expected and observed exclusion limits for an axial vector coupling mediator model. Left: M_χ= 1 GeV. Right: M_χ= 50 GeV.

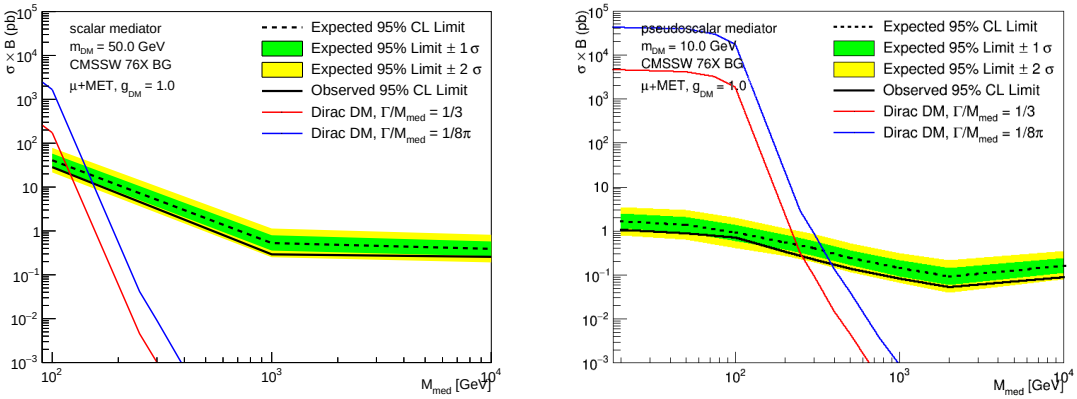

Figure 24: M_{med}-dependent expected and observed exclusion limits. Left: Scalar coupling mediator model for M_χ= 50 GeV. Right: Pseudoscalar coupling mediator model with M_χ= 10 GeV.

is no intersection and hence exclusion limits cannot be set in the AV for $M_\chi = 50$ GeV and $\Gamma = \frac{M_{med}}{3}$.

On one hand, the Fig. 23 left presents a shallow shape, this means that an increment on the luminosity would significantly increase the range of mediator masses to which we are sensible. On the other hand, both plots of Fig. 24 show a steeply falling curve, therefore, an increase on the amount of data (*i. e.*increase in luminosity) will not improve substantially the sensitivity to the mediator mass of this analysis. This abrupt falling in the scalar and pseudoscalar coupling mediators is due because the off-shell W boson have to be heavy enough to produce the χ, $\bar{\chi}$ pair and another W boson. That is why the fall is starting in the point where M_{med} is approximately the same as the W boson.

The Fig. 23 right presents a threshold where the mediator mass is approximately twice the dark matter mass, just after this point there is a resonance[19] for the narrow width case. For the conservative width there is also an increase on the cross section but is not so prominent.

[19] Increase in the cross section.

4.11.2 Exclusion limits in the simplified model parameter space

The two-dimensional plots exclude a range of DM and mediator masses for each model by establishing upper limits. With the intersection points between the theoretical curves with the observed and expected ones of the simple limits plot we can make an interpolation and create two-dimensional limit plots. If there are two intersections, the one corresponding to a lower mediator mass is considered. This plots show the M_{med} in the horizontal axes and the M_χ in the vertical one. With the interpolation a closed curve is drawn in the plots and the points (M_{med}, M_χ) inside the curve are excluded from the model. The black dots correspond to the points where the cross section has been calculated.

In the Fig. 25, the exclusion limits in the AV parameter space are shown. Mediator masses below[20] 400 GeV and 80 GeV were excluded for the narrow width and conservative approaches respectively. Depending on the value of the the dark matter mass, the exclusion on the mediator mass can be different. For low M_χ we have the maximum exclusion on M_{med}. For M_χ above 160 GeV there is no exclusion on the M_{med} for the $\Gamma = M_{med}/8\pi$ and 20 GeV for the $\Gamma = M_{med}/3$.

When the limits in one dimension were set, the AV model presented more intersection than the S and P. For the last two, only one intersection was found for each mediator width and hence the closed curve draws a triangle –Fig. 26– in both cases. For the S coupling the mediator excluded masses are 153 GeV for the narrow width and 121 GeV for the conservative. For the P, 379 GeV for the narrow width and 254 GeV for the conservative are excluded from the model.

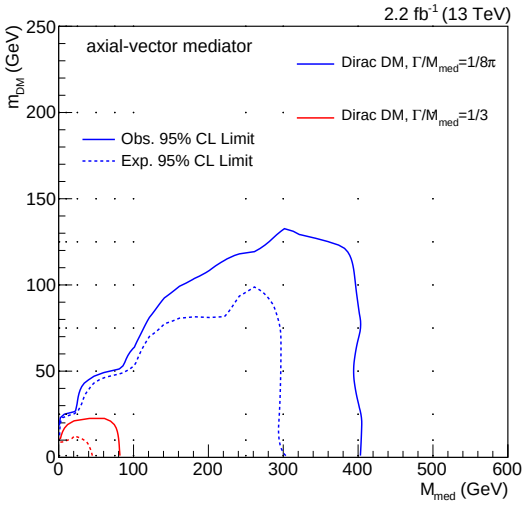

Figure 25: Two dimensional representation of the production cross section in the $M_{med} - M_\chi$ plane for an axial vector coupling.

[20] Not all masses below, only the ones inside the curves.

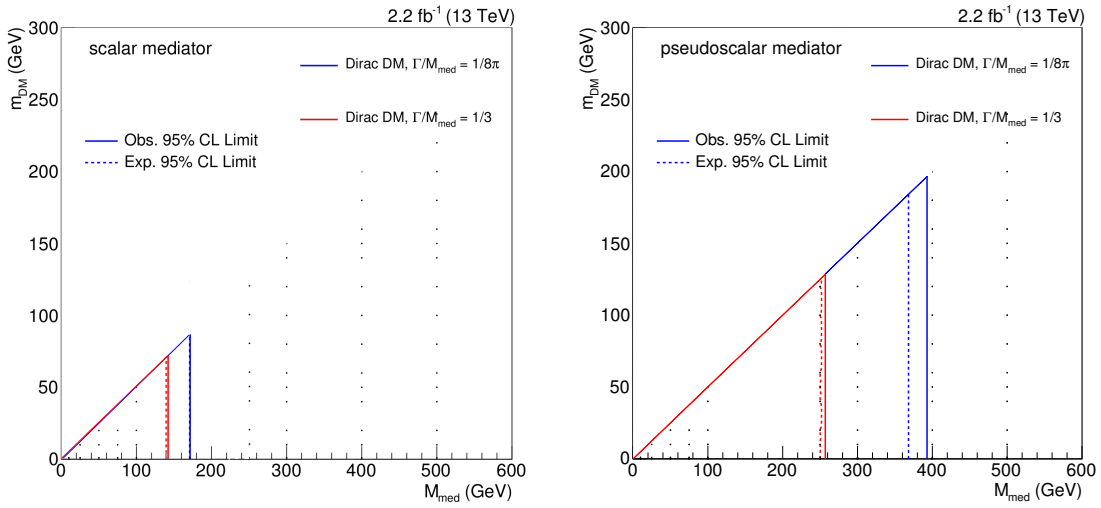

Figure 26: Two dimensional representation of the production cross section in the $M_{med} - M_{\chi}$ plane. Left: Scalar coupling model. Right: Pseudo scalar coupling model.

5 Summary and outlook

It is important to mention that this is the first analysis done using simplified models for the $\mu + E_T^{miss}$. During Run I the $\mu + E_T^{miss}$ was researched using data corresponding to center of mass energy of 8 TeV, therefore it was studied with the effective field theory (EFT) approach. This implies that this thesis is also the first analysis for the $\mu + E_T^{miss}$ that consider the scalar and pseudoscalar couplings because the EFT approach[21] only used vector and axial vector couplings. These simplified models have also been recently used with the Run II data but it was done the $e + E_T^{miss}$. [47]

While no evidence for new physics has been found, constraints on the mass of the dark matter parameter space have been set. For the axial vector model, mediator masses up to 400 GeV have been excluded. Simplified models provide an opportunity to study scalar and pseudoscalar coupling mediators. Mediator masses up to 153 GeV can be excluded for scalar coupling. For pseudoscalar coupling, mediator masses up to 379 GeV can be excluded. For the last two couplings, those are the first results in the muon channel. In the electron channel, the mediator masses were excluded up to 550 GeV for the axial vector 150 GeV for the scalar and 400 GeV for the pseudoscalar [21]. Those limits depend on the dark matter mass as is shown in figures 25 and 26.

By 2025, the High Luminosity LHC upgrade project will provide the CMS and additional integrated luminosity of 2500 fb$^-$1. This will substantially enlarge the mass reach in the search for new particles [48]. This will enhance the sensitivity to dark matter search and, consequently, the research in the parameter space. For axial-vector coupling simplified models and a narrow width approach, it can potentially probe beyond heavy mediator masses of 5 TeV [21].

[21] The EFT is the model that has been used in previous works. It does not consider the mediator particle.

Acknowledgments

During the realization of this thesis I have benefit from the help of many others and hence I would like to conclude with acknowledgments for those who have supported me.

First of all, I have to thank Klaas Padeken, Viktor Kutzner, Fabian Bispinck and Marcel Materok for their mentoring, patience and unflagging support during all these months. Without your collaboration nothing would be possible.

My most sincere gratitude to Dr. Kerstin Hopfner for the opportunity to study this interesting subject, her advice and making it possible for me to write this thesis.

I would also like to thank Alberto Escalante for the scripts for fixing of muon scale.

Also, thanks to Pau, Cail, Shreyas, Gab and Sandra for their helpful comments, corrections and opinions about this work.

Finally, my most honest thanks to my mother, who made it possible for me to study physics. *Gràcies per donar-ho tot pels teus fills des del primer moment.*

A Appendices

A.1 Coordinate system

The coordinate system adopted by CMS has the origin centered at the collision point, the Y axis is pointing vertically upward, the X axis pointing radially inward toward the center of the LHC circumference and, finally, the Z axis points along the beam direction toward the surface. The azimuthal angle ϕ is measured from the X axis in the XY plane and the radial coordinate in this plane is denoted by r . The polar angle θ is measured from the Z axis but typically, instead of using θ , the pseudorapidity is used: $\eta = -ln(tan\frac{\theta}{2})$. All the transverse quantities are defined in the XY plane.

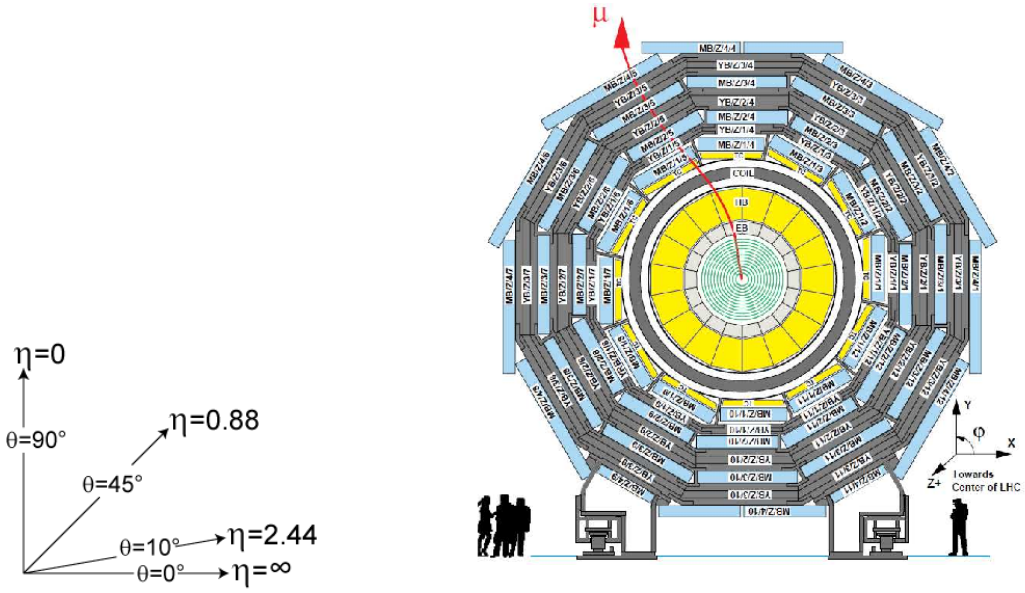

Figure 27: Left: Correspondence between the θ angle and the pseudorapidity, η [49]. Right: Transversal view of CMS [50].

A.2 Event display

Figs. 28 and 29 show the event display exhibiting the largest M_T measured in the mono-μ channel. The former show the muon and E_T^{miss} in the transverse plane of CMS detector. The latest is a the three-dimensional view of the same event.

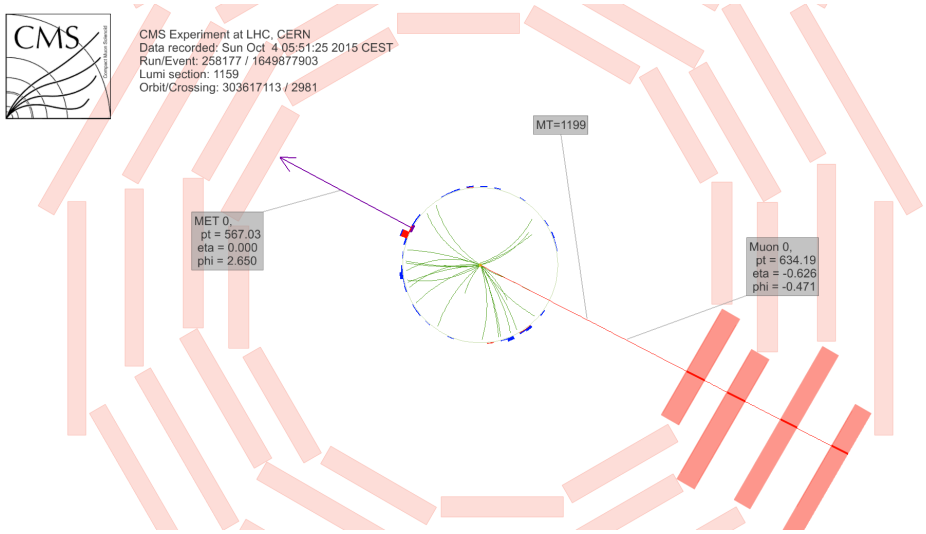

Figure 28: Event display showing in the transverse plane the event with the highest transverse mass, M_T = 1199 GeV in the single muon channel. The muon has a tranverse momentum of p_T= 634 GeV.

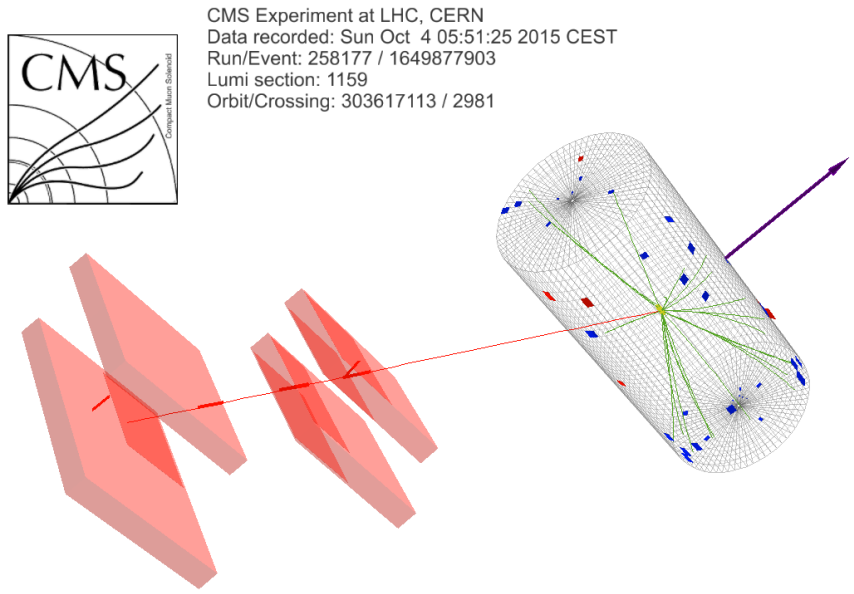

Figure 29: Event display showing the event with the highest transverse mass, M_T = 1199 GeV in the single muon channel. The muon has a tranverse momentum of p_T= 634 GeV.

A.3 Acronyms

ALICE – A Large Ion Collider Experiment
ATLAS – A Toroidal LHC Apparatus
AV – Axial Vector
BSM – Beyond the Standard Model
CERN – European Organization for Nuclear Research
CIEMAT – Centro de Investigaciones Energéticas, Medioambientales y Tecnológicas
CL – Confidence level
CMB – cosmic microwave background
COBE – Cosmic Background Explorer
CP – Charge Parity
CSC – Cathode strip chamber
DM – Dark Matter
DT – Drift tubes
ECAL – Electromagnetic calorimeter
ESA – European Space Agency
FSR – Final state radiation
HB – Hadronic barrel
HCAL – Hadronic calorimeter
HE – Hadronic endcap
HF – Hadronic forward calorimeter
HLT – High level trigger
HO – Hadronic outer calorimeter
ISR – Initial state radiation
L1 – Level one trigger
LHC – Large Hadron Collider
LHCb – Large Hadron Collider beauty
LHCf – Large Hadron Collider forward

LO – Leading Order
Lambda-CDM – Lambda cold dark matter
MC – Monte Carlo
MOND – Modified Newtonian Dynamics
MoEDAL – Monopole & Exotics Detector at the LHC
NASA – National Aeronautics and Space Administration
NLO – Next to Leading Order
NNLO – Next to Next to Leading Order
P – Pseudoscalar
PDF – Parton Distribution Functions
PS – Proton Synchrotron
PSB – Proton Synchrotron Booster
PXLIO – Physics eXtension Library Input Output format
RF – Radiofrequency
RPC – Resistive plate chamber
S – Scalar
SM – Standard Model
SPS – Super Proton Synchrotron
TEC – Tracker Endcap
TIB – Tracker Inner Barrel
TID – Tracker Inner Disk
TOB – Tracker Outer Barrel
TOTEM – TOTal cross section, Elastic scattering and diffraction dissociation Measurement at the LHC
V – Vector
WIMP – weakly interacting massive particle
WLCG – Worldwide LHC Computing Grid
WMAP – Wilkinson Microwave Anisotropy Probe

References

[1] C. C. W. Taylor *et al.*, *The atomists, Leucippus and Democritus: fragments: a text and translation with a commentary*, vol. 5. University of Toronto Press, 2010.

[2] O. Leaman, *Key concepts in Eastern philosophy*. Routledge, 2002.

[3] **DONUT** Collaboration, "Observation of tau neutrino interactions", *Phys. Lett.B* **504** (2001) 218–224, arXiv:hep-ex/0012035 [hep-ex].

[4] Wikipedia, "Standard model — Wikipedia, the free encyclopedia", 2016. https://en.wikipedia.org/wiki/Standard_Model.

[5] J. H. Oort, "The force exerted by the stellar system in the direction perpendicular to the galactic plane and some related problems", *Bulletin of the Astronomical Institutes of the Netherlands* **6** (1932) 249.

[6] F. Zwicky, "Spectral displacement of extra galactic nebulae", *Helv. Phys. Acta* **6** no. 110-127, (1933) 15.

[7] F. Zwicky, "On the masses of nebulae and of clusters of nebulae", *The Astrophysical Journal* **86** (1937) 217.

[8] V. C. Rubin, "Dark matter in spiral galaxies", *Scientific American* **248** (June, 1983) 96–106.

[9] A. G. Bergmann, V. Petrosian, and R. Lynds, "Gravitational lens models of arcs in clusters", *The Astrophysical Journal* **350** (1990) 23–35.

[10] Wikipedia, "Galaxy rotation curve — Wikipedia, the free encyclopedia", 2016. https://en.wikipedia.org/wiki/Galaxy_rotation_curve.

[11] K. Garrett and G. Duda, "Dark Matter: A Primer", *Adv. Astron.* **2011** (2011) 968283, arXiv:1006.2483 [hep-ph].

[12] **Planck** Collaboration, "Planck 2013 results. I. Overview of products and scientific results", *Astron. Astrophys.* **571** (2014) A1, arXiv:1303.5062 [astro-ph.CO].

[13] D. Clowe, M. Bradač, A. H. Gonzalez, M. Markevitch, S. W. Randall, C. Jones, and D. Zaritsky, "A direct empirical proof of the existence of dark matter.", *The Astrophysical Journal Letters* **648** no. 2, (2006) L109.

[14] N. F. Bell, Y. Cai, J. B. Dent, R. K. Leane, and T. J. Weiler, "Dark matter at the LHC: Effective field theories and gauge invariance", *Physical Review D* **92** no. 5, (2015) 053008.

[15] K. Griest, "The Search for dark matter: WIMPs and MACHOs", arXiv:hep-ph/9303253 [hep-ph].

[16] J. M. Gaskins, "A review of indirect searches for particle dark matter", *Contemporary Physics* (2016) 1–30.

[17] **ATLAS and CMS** Collaboration, "Dark Matter Benchmark Models for Early LHC Run-2 Searches: Report of the ATLAS/CMS Dark Matter Forum", arXiv:1507.00966 [hep-ex].

[18] C. O'Luanaigh, "Extra dimensions, gravitons, and tiny black holes",. http://cds.cern.ch/record/1997197.

[19] P. Harris, V. Khoze, M. Spannowsky, and C. Williams, "Constraining dark sectors at colliders: beyond the effective theory approach", *Physical Review D* **91** no. 5, (2015) 055009.

[20] **CMS** Collaboration, "Search for physics beyond the standard model in final states with a lepton and missing transverse energy in proton-proton collisions at $\sqrt{s} = 8$ TeV", *Phys. Rev. D* **91** no. 9, (2015) 092005, arXiv:1408.2745 [hep-ex].

[21] V. Kutzner, "Search for new physics in the mono-electron channel with the CMS experiment in pp collision data at $\sqrt{s}$=13 TeV, Master thesis", 2016.

[22] P. J. Fox, R. Harnik, J. Kopp, and Y. Tsai, "Missing energy signatures of dark matter at the LHC", *Phys. Rev. D* **85** (Mar, 2012) 056011. http://link.aps.org/doi/10.1103/PhysRevD.85.056011.

[23] P. J. Fox, R. Harnik, J. Kopp, and Y. Tsai, "Missing Energy Signatures of Dark Matter at the LHC", *Phys. Rev.* **D85** (2012) 056011, arXiv:1109.4398 [hep-ph].

[24] L. Evans and P. Bryant, "LHC Machine", *JINST* **3** (2008) S08001.

[25] C. Pralavorio, "LHC performance reaches new highs", 2016. http://cds.cern.ch/record/2203203.

[26] C. O'Luanaigh, "Experiments",. http://cds.cern.ch/record/1997374.

[27] J. Nielsen, "Fundamentals of LHC Experiments", in *Proceedings, Theoretical Advanced Study Institute in Elementary Particle Physics (TASI 2010). String Theory and Its Applications: From MeV to the Planck Scale: Boulder, Colorado, USA, June 1-25, 2010*, pp. 127–152. 2011. arXiv:1106.2516 [hep-ex]. https://inspirehep.net/record/913551/files/arXiv:1106.2516.pdf.

[28] **CMS** Collaboration, "The CMS experiment at the CERN LHC", *JINST* **3** (2008) S08004.

[29] T. Sakuma and T. McCauley, "Detector and Event Visualization with SketchUp at the CMS Experiment", *J. Phys. Conf. Ser.* **513** (2014) 022032, arXiv:1311.4942 [physics.ins-det].

[30] **CMS** Collaboration, "MiniAOD Analysis Documentation — TWiki, CERN", 2016. https://twiki.cern.ch/twiki/bin/view/CMSPublic/WorkBookMiniAOD2015.

[31] H. P. Bretz *et al.*, "A Development Environment for Visual Physics Analysis", *JINST* **7** (2012) T08005, arXiv:1205.4912 [physics.data-an].

[32] K. Padeken, *Search for new physics in the tau plus missing energy and other mono lepton final states at CMS*. PhD thesis. RWTH Aachen, 2016.

[33] **Particle Data Group** Collaboration, K. A. Olive *et al.*, "Review of Particle Physics", *Chin. Phys.* **C38** (2014) 090001.

[34] **CMS** Collaboration, M. Olschewski, K. Padeken, and K. Hoepfner, "Cross section calculation for leptonically decaying W at NNLO QCD and NLO electroweak", tech. rep., 2014. CMS-AN-14-263.

[35] Wikipedia, "Sagitta (geometry) — Wikipedia, the free encyclopedia", 2016. `https://en.wikipedia.org/wiki/Sagitta_%28geometry%29`.

[36] J. Hauptman, *Particle physics experiments at high energy colliders*. John Wiley & Sons, 2011.

[37] R. Frühwirth, "Application of kalman filtering to track and vertex fitting", *Nuclear Instruments and Methods in Physics Research Section A: Accelerators, Spectrometers, Detectors and Associated Equipment* **262** no. 2, (1987) 444–450.

[38] M. Olschewski, *Search for new physics in proton-proton collision events with a lepton and missing transverse energy*. Dr., RWTH Aachen, Aachen, 2016. `https://publications.rwth-aachen.de/record/572409`. Veroeffentlicht auf dem Publikationsserver der RWTH Aachen University; Dissertation, RWTH Aachen, 2016.

[39] **CMS** Collaboration, "Search for SSM W' production, in the lepton+MET final state at a center-of-mass energy of 13 TeV",. PAS-EXO-15-006.

[40] **CMS** Collaboration, S. Chatrchyan *et al.*, "Performance of CMS muon reconstruction in *pp* collision events at $\sqrt{s} = 7$ TeV", *JINST* **7** (2012) P10002, `arXiv:1206.4071 [physics.ins-det]`.

[41] S. van der Meer, "Calibration of the effective beam height in the ISR",. `https://cds.cern.ch/record/296752`.

[42] **CMS** Collaboration, "Pile up JSON File for dat — TWiki, CERN", 2016. `https://twiki.cern.ch/twiki/bin/viewauth/CMS/PileupJSONFileforData`.

[43] R. P. Feynman, "The behavior of hadron collisions at extreme energies", in *Special Relativity and Quantum Theory*, pp. 289–304. Springer, 1988.

[44] J. Butterworth *et al.*, "PDF4LHC recommendations for LHC Run II", *J. Phys.* **G43** (2016) 023001, `arXiv:1510.03865 [hep-ph]`.

[45] G. Cowan, K. Cranmer, E. Gross, and O. Vitells, "Asymptotic formulae for likelihood-based tests of new physics", *Eur. Phys. J.* **C71** (2011) 1554, `arXiv:1007.1727 [physics.data-an]`. [Erratum: Eur. Phys. J.C73,2501(2013)].

[46] **RooStats Team** Collaboration, G. Schott, "RooStats for Searches", in *Proceedings, PHYSTAT 2011 Workshop on Statistical Issues Related to Discovery Claims in Search Experiments and Unfolding, CERN,Geneva, Switzerland 17-20 January 2011*, pp. 199–208, CERN. CERN, Geneva, 2011. `arXiv:1203.1547 [physics.data-an]`.

[47] M. Materok, "Search for dark matter with scalar or pseudoscalar coupling in Run 2 data. Bachelor thesis",. `https://web.physik.rwth-aachen.de/~hebbeker/theses/materok_bachelor.pdf`.

[48] D. Contardo, M. Klute, J. Mans, L. Silvestris, and J. Butler, "Technical Proposal for the Phase-II Upgrade of the CMS Detector", Tech. Rep. CERN-LHCC-2015-010. LHCC-P-008. CMS-TDR-15-02, Geneva, Jun, 2015. https://cds.cern.ch/record/2020886.

[49] Wikipedia, "Pseudorapidity — Wikipedia, the free encyclopedia", 2015. https://en.wikipedia.org/wiki/Pseudorapidity.

[50] **CMS** Collaboration, "Performance of the CMS Drift Tube Chambers with Cosmic Rays", *JINST* **5** (2010) T03015, arXiv:0911.4855 [physics.ins-det].